

Numerical Simulations of Highly Porous Dust Aggregates in the Low-Velocity Collision Regime

Implementation and Calibration of a Smooth Particle Hydrodynamics Code

R. J. Geretshauser¹, R. Speith¹, C. Güttler², M. Krause², and J. Blum²

¹ Institut für Astronomie und Astrophysik, Abteilung Computational Physics, Eberhard Karls Universität Tübingen, Auf der Morgenstelle 10, D-72076 Tübingen, Germany

e-mail: ralf.j.geretshauser@uni-tuebingen.de

² Institut für Geophysik und extraterrestrische Physik, Technische Universität zu Braunschweig, Mendelssohnstr. 3, D-38106 Braunschweig, Germany

Preprint online version: January 11, 2010; accepted by *Astronomy & Astrophysics* December 22, 2009

ABSTRACT

Context. A highly favoured mechanism of planetesimal formation is collisional growth. Single dust grains hit each other due to relative velocities caused by gas flows in the protoplanetary disc, which they follow. They stick due to van der Waals forces and form fluffy aggregates up to centimetre size. The mechanism of further growth is unclear since the outcome of aggregate collisions in the relevant velocity and size regime cannot be investigated in the laboratory under protoplanetary disc conditions. Realistic statistics of the result of dust aggregate collisions beyond decimetre size is missing for a deeper understanding of planetary growth.

Aims. Joining experimental and numerical efforts we want to calibrate and validate a computer program that is capable of a correct simulation of the macroscopic behaviour of highly porous dust aggregates. After testing its numerical limitations thoroughly we will check the program especially for a realistic reproduction of the compaction, bouncing and fragmentation behaviour. This will demonstrate the validity of our code, which will finally be utilised to simulate dust aggregate collisions and to close the gap of fragmentation statistics in future work.

Methods. We adopt the smooth particle hydrodynamics (SPH) numerical scheme with extensions for the simulation of solid bodies and a modified version of the Sirono porosity model. Experimentally measured macroscopic material properties of SiO₂ dust are implemented. By simulating three different setups we calibrate and test for the compressive strength relation (compaction experiment) and the bulk modulus (bouncing and fragmentation experiments). Data from experiments and simulations will be compared directly.

Results. SPH has already proven to be a suitable tool to simulate collisions at rather high velocities. In this work we demonstrate that its area of application can not only be extended to low-velocity experiments and collisions. It can also be used to simulate the behaviour of highly porous objects in this velocity regime to a very high accuracy. A correct reproduction of density structures in the compaction experiment, of the coefficient of restitution in the bouncing experiment and of the fragment mass distribution in the fragmentation experiment show the validity and consistency of our code for the simulation of the elastic and plastic properties of the simulated dust aggregates. The result of this calibration process is an SPH code that can be utilised to investigate the collisional outcome of porous dust in the low-velocity regime.

Key words. hydrodynamics - methods: laboratory - methods: numerical - planets and satellites: formation - planetary systems: formation - planetary systems: protoplanetary disks

1. Introduction

In gaseous circumstellar discs, the potential birthplace of planetary systems, dust grains smaller than a micrometre grow to kilometre-sized planetesimals, which themselves proceed to terrestrial planets and cores of giant planets by gravity-driven runaway accretion. Depending on their size the dust grains and aggregates perform motions in the disc and relative to each other. Brownian motion, radial drift, vertical settling and turbulent mixing cause mutual collisions (Weidenschilling 1977; Weidenschilling & Cuzzi 1993).

Since real protoplanetary dust particles are not available for experiments in the laboratory much of the following work has been carried out with dust analogues such as SiO₂ (Blum & Wurm 2008). Theoretical models also refer to microscopic and macroscopic properties of these materials. Initially the dust grains hit and stick on contact by van der Waals forces

(Heim et al. 1999). In this process, which has been investigated experimentally (Blum et al. 2000; Blum & Wurm 2000; Krause & Blum 2004) and numerically (Dominik & Tielens 1997; Paszun & Dominik 2006, 2008, 2009; Wada et al. 2007, 2008, 2009), they form fluffy aggregates with a high degree of porosity.

Due to restructuring the aggregates gain a higher mass to surface ratio and reach higher velocities. Blum & Wurm (2000, 2008) and Wada et al. (2008) showed that collisions among them lead to fragmentation and mass loss. Depending on the model of the protoplanetary disc, which provides the kinetic collision parameters, this means that direct growth ends at aggregate sizes of a few centimetres. However, Wurm et al. (2005) and Teiser & Wurm (2009) have demonstrated in laboratory experiments in the centimetre regime and with low-porosity dust that the projectile can stick partially to the target at velocities of

more than 20 m s^{-1} . Thus, collisional growth beyond centimetre size seems to be possible and the exact outcome of the fragment distribution is crucial for the understanding of the growth mechanism.

Numerical models that try to combine elaborate protoplanetary disc physics with the dust coagulation problem (Weidenschilling et al. 1997; Dullemond & Dominik 2005; Brauer et al. 2008; Zsom & Dullemond 2008; Ormel et al. 2007, 2009) have to make assumptions about the outcome of collisions between dusty objects for all sizes and relative velocities. Since data for these are hardly available, in the most basic versions of these models perfect sticking, in more elaborate ones power-law fragment distributions from experiments and observations (Mathis et al. 1977; Davis & Ryan 1990; Blum & Münch 1993) are assumed. The results of alike simulations highly depends on the assumed fragmentation kernel. However, the given experimental references have been measured only for small aggregate sizes. The influence of initial parameters such as the rotation of the objects or their porosity have not been taken into account for the size regimes beyond centimetre size, although they might play an important role (Sirono 2004; Ormel et al. 2007).

A new approach to model the growth of protoplanetary dust aggregates was recently developed by Güttler et al. (2009a) and Zsom et al. (2009) who directly implemented the results of dust aggregation experiments into a Monte-Carlo growth model. They found that bouncing of protoplanetary dust aggregates plays a major role for their evolution as it is able to inhibit further growth and changes their aerodynamic properties. Although their model relies on the most comprehensive database of dust aggregate properties and their collisional behaviour, they were unable to make direct predictions for any arbitrary set of collision parameters and were thus obliged to perform extrapolations over orders of magnitude. Some of these extrapolations are based on physical models which need to be supported by further experiments and where this is not possible by sophisticated numerical models such as the one presented here.

Sticking, bouncing, and fragmentation are the important collision outcomes which need to be implemented into a coagulation code and affect the results of these models. Thus, it is not only important to correctly implement the exact thresholds between these regimes but also details concerning the outcome such as the fragment size distribution, the compaction in bouncing collisions, and maybe even the shape of the aggregates after they merged in a sticking collision. Due to the lack of important input information the necessity for a systematic study of all relevant collision parameters arises and will be addressed in this work.

Because of restrictions in size and realistic environment parameters this task cannot be achieved in the laboratory alone. There has been a lot of work lately on modelling the behaviour of dust aggregates on the basis of molecular interactions between the monomers (Paszun & Dominik 2006, 2008, 2009; Wada et al. 2007, 2008, 2009). However, simulating dust aggregates with a model based on macroscopic material properties such as density, porosity, bulk and shear moduli and compressive, tensile and shear strengths remains an open field since these quantities are rarely available. The advantage of this approach over the molecular dynamics method, which is computationally limited to a few ten thousand monomers, is the accessibility of aggregate sizes beyond the centimetre regime.

Recently, Jutzi et al. (2008) have implemented a porosity model into the smooth particle hydrodynamics (SPH) code by Benz & Asphaug (1994). It was calibrated for pumice material using high-velocity impact experiments (Jutzi et al.

2009b) and utilised to understand the formation of an asteroid family (Jutzi et al. 2009a). However, pumice is a material whose strength parameters decrease when it is compacted (crushed). Additionally, the underlying thermodynamically enhanced porosity model is designed to describe impacts of some km s^{-1} . Thus, it is perfectly suitable to simulate high-velocity collisions of porous rock-like material.

In contrast, collisions between pre-planetesimals occur at relative velocities of some tens of m s^{-1} and compressive, shear and tensile strengths are increasing with increasing density (Blum & Schräpler 2004; Blum et al. 2006; Güttler et al. 2009b).

Schäfer et al. (2007) have used an SPH code based on the porosity model by Sirono (2004) to simulate collisions between porous ice in the m s^{-1} regime. They found that a suitable choice of relations for the material parameters can produce sticking, bouncing or fragmentation of the colliding objects. Therefore, they stressed the importance of calibrating the material parameters of porous matter with laboratory measurements. Numerical molecular-dynamics simulations are about to use a sufficient number of monomers to be close enough to the continuum limit and to provide the required material parameters (e.g. Paszun & Dominik 2008, reproducing experimental results of Blum & Schräpler 2004). They represent an important support to the difficult experimental determination of these quantities. In Güttler et al. (2009b) we have measured the compressive strength relation for spherical SiO_2 dust aggregates for the static case in the laboratory and have given a prescription how to apply this to the dynamic case using a compaction calibration experiment and 2D simulations. We have pointed out relevant benchmark features. It was shown that the code is in principal capable of simulating not only fragmentation but also bouncing, which cannot be seen in molecular-dynamics codes so far.

In this work we present our SPH code with its technical details (Sect. 2), experimental reference (Sect. 3), and numerical properties (Sect. 4). On the basis of the compaction calibration simulation we demonstrate that the results converge for increasing spatial resolution and choose a sufficient numerical resolution (Sect. 4.2). We investigate the differences between 2D and 3D numerical setup (Sect. 4.3) and thereby improve some drawbacks in Güttler et al. (2009b). Artificial viscosity will be presented as stabilising tool for various problems in the simulations and its influence on the physical results will be pointed out (Sect. 4.4).

Most prominently we continue the calibration process started in Güttler et al. (2009b) utilising two further calibration experiments for bouncing (Sect. 5.2) and fragmentation (Sect. 5.3). In the end we possess a collection of material parameters, which is consistent for all benchmark experiments. Finally, the SPH code has gained enough reliability to be used to enhance our information about the underlying physics of dust aggregate collisions beyond the centimetre regime. In future work it will be applied to generate a catalogue of pre-planetesimal collisions and their outcome regarding all relevant parameters for planet formation. Jointly with experiments and coagulation models this can be implemented into protoplanetary growth simulations (Güttler et al. 2009a; Zsom et al. 2009) to enhance their reliability and predictive power.

2. Physical Model and Numerical Method

2.1. Smooth Particle Hydrodynamics

The numerical Lagrangian particle method smooth particle hydrodynamics (SPH) was originally introduced by Lucy (1977) and Gingold & Monaghan (1977) to model compressible hydrodynamic flows in astrophysical applications. Later, the method has been extended (Libersky & Petschek 1990), and improved extensively (e.g. Libersky et al. 1993; Benz & Asphaug 1994; Randles & Libersky 1996; Libersky et al. 1997) to simulate elastic and plastic deformations of solid materials. A comprehensive description of SPH and its extensions can be found in Monaghan (2005).

In the SPH scheme, continuous solid objects are discretized into interacting mass packages, so called “particles”. These particles form a natural frame of reference for any deformation and fragmentation that the solid body may undergo. All spatial field quantities of the object are approximated onto the particle positions \mathbf{x}_i by a discretized convolution with a kernel function W . The kernel W depends on particle distance $|\mathbf{x}_j - \mathbf{x}_i|$ and has compact support, determined by the smoothing length h . We are using the standard cubic spline kernel (Monaghan & Lattanzio 1985) but normalised such that its maximum extension is equal to one smoothing length h .

We apply a constant smoothing length. This also allows to model fragmentation of solid objects in a simple way. Fragmentation occurs when some SPH particles within the body lose contact with their adjacent particles. Two fragments are completely separated as soon as their respective subsets of particles have reached a distance of more than $2h$ so that their kernels do not overlap any more.

Time evolution of the SPH particles is computed according to the Lagrangian form of the equations of continuum mechanics, while transferring spatial derivatives by partial integration onto the analytically given kernel W .

2.2. Continuum mechanics

A system of three partial differential equations forms the framework of continuum mechanics. As commonly known they follow from the constraints of conservation of mass, momentum and energy. The first, accounting for the conservation of mass, is called continuity equation

$$\frac{d\rho}{dt} + \rho \frac{\partial v^\alpha}{\partial x^\alpha} = 0. \quad (1)$$

Following the usual notation ρ and v^α denote density and velocity, respectively. Greek indices run from 1 to d , the dimension of the problem. Einstein summing notation holds throughout the entire paper. In contrast to the usual SPH scheme, where the SPH density ρ_i is calculated directly from the particle distribution, we solve the continuity equation according to

$$\frac{d\rho_i}{dt} = -\rho_i \sum_j \frac{m_j}{\rho_j} (v_j^\alpha - v_i^\alpha) \frac{\partial W^{ij}(h)}{\partial x_i^\alpha} \quad (2)$$

(e.g. Randles & Libersky 1996). Here the sum runs over all interaction partners j of particle i , m_j is the particle mass of particle j , and W^{ij} denotes the kernel for the particular interaction. Although this approach is more expensive, as it requires to solve an additional ordinary differential equation for each particle, it is more stable for high density contrasts and it avoids artifacts due to smoothing at boundaries and interfaces.

The conservation of momentum is ensured by the second equation

$$\frac{dv^\alpha}{dt} = \frac{1}{\rho} \frac{\partial \sigma^{\alpha\beta}}{\partial x^\beta}. \quad (3)$$

In SPH formulation, the momentum equation reads

$$\frac{dv_i^\alpha}{dt} = \sum_j m_j \left(\frac{\sigma_i^{\alpha\beta}}{\rho_i^2} + \frac{\sigma_j^{\alpha\beta}}{\rho_j^2} \right) \frac{\partial W^{ij}(h)}{\partial x_i^\beta}. \quad (4)$$

Due to the symmetry in the interaction terms, conservation of momentum is ensured by construction. Additionally we apply the standard SPH artificial viscosity (Monaghan & Gingold 1983). This is essential in particular for stability at interfaces with highly varying densities. The influence of artificial viscosity on our simulation results is investigated thoroughly in Sec. 4.4.

The third equation, the energy equation, is not used in our model. Hence, we assume that kinetic energy is mainly converted into deformation energy and energy dissipated by viscous effects is converted into heat and radiated away. The stress tensor σ can be split into a part representing the pure hydrostatic pressure p and a traceless part for the shear stresses, the so called deviatoric stress tensor $S^{\alpha\beta}$. Hence,

$$\sigma^{\alpha\beta} = -p\delta^{\alpha\beta} + S^{\alpha\beta}. \quad (5)$$

Any deformation of a solid body leads to a development of internal stresses in a specifically material dependent manner. The relation between deformation and stresses is not taken into account within the regular equations of fluid dynamics. Therefore, they are insufficient to describe a perfectly elastic body and have to be extended. The missing relations are the constitutive equations, which depend on the strain tensor

$$\epsilon^{\alpha\beta} = \frac{1}{2} \left(\frac{\partial x'^\alpha}{\partial x^\beta} + \frac{\partial x'^\beta}{\partial x^\alpha} \right). \quad (6)$$

It represents the local deformation of the body. The primed coordinates denote the positions of the deformed body.

Following Hooke’s law a proportional relation between deformation is assumed involving the material dependent shear modulus $\mu = \mu(\rho)$, which depends itself on the density:

$$S^{\alpha\beta} \propto 2\mu \left(\epsilon^{\alpha\beta} - \frac{1}{d} \delta^{\alpha\beta} \epsilon^{\gamma\gamma} \right). \quad (7)$$

However, this is only the constitutive equation for the traceless shear part. For the hydrostatic part of the stress tensor we adopt a modification of the Murnaghan equation of state which is part of the Sirono (2004) porosity model:

$$p(\rho) = K(\rho'_0)(\rho/\rho'_0 - 1), \quad (8)$$

where ρ'_0 is the so called reference density, the density of the material at zero external stress, and $K(\rho)$ is the bulk modulus.

The density dependence of the bulk $K(\rho)$ and shear $\mu(\rho)$ moduli is modelled by a power law

$$K(\rho) = 2\mu(\rho) = K_0(\rho/\rho_i)^\gamma. \quad (9)$$

Although according to Sirono (2004) ρ_i is the initial density of the material at the beginning of the simulation, we, in contrast, want to ensure that our dust material possesses the same bulk modulus $K(\rho)$ even for simulations with different initial densities. In this work the dust material has two different densities

at the beginning of the bouncing (Sect. 5.2) and fragmentation (Sect. 5.3) calibration setup. According to Sirono (2004) the materials should feature two different ρ_i . As a consequence $K(\rho)$, and in particular K_0 , depends on the initial setup. Since we want to compare and validate K_0 by using two different setups we have to fix a unique ρ_i for all simulations. We choose ρ_i such that $K(\rho_i) = K_0$ is the bulk modulus of the generic uncompressed dust material that is produced by the random ballistic deposition (RBD) method (Blum & Schr apler 2004).

The time evolution of the pressure is directly given by the time evolution of the density (Eq. 1) and since the pressure is a scalar quantity it is intrinsically invariant under rotation. However, in order to gain a frame invariant formulation of the time evolution of the deviatoric stress tensor, i.e. the stress rate, correction terms have to be added. A very common formulation for SPH (see e.g. Benz & Asphaug 1994; Sch afer et al. 2007) is the Jaumann rate form

$$\frac{dS^{\alpha\beta}}{dt} = 2\mu \left(\dot{\epsilon}^{\alpha\beta} - \frac{1}{d} \delta^{\alpha\beta} \dot{\epsilon}^{\gamma\gamma} \right) + S^{\alpha\gamma} R^{\gamma\beta} + S^{\beta\gamma} R^{\gamma\alpha}, \quad (10)$$

where $R^{\alpha\beta}$ is the rotation rate tensor, defined by

$$R^{\alpha\beta} = \frac{1}{2} \left(\frac{\partial v^\alpha}{\partial x^\beta} - \frac{\partial v^\beta}{\partial x^\alpha} \right) \quad (11)$$

and $\dot{\epsilon}^{\alpha\beta}$ denotes the strain rate tensor

$$\dot{\epsilon}^{\alpha\beta} = \frac{1}{2} \left(\frac{\partial v^\alpha}{\partial x^\beta} + \frac{\partial v^\beta}{\partial x^\alpha} \right). \quad (12)$$

To determine rotation rate and strain rate tensor and thus the evolution of the stress tensor Eq. 10 in SPH representation, the SPH velocity derivatives $\partial v_i^\alpha / \partial x_i^\beta$ have to be calculated. The standard SPH formulation, however, does not conserve angular momentum due to the discretization error by particle disorder, which leads to a rotational instability and in particular inhibits modelling rigid rotation of solid bodies. To avoid this error, we apply a correction tensor $C^{\gamma\beta}$ (Sch afer et al. 2007) according to

$$\frac{\partial v_i^\alpha}{\partial x_i^\beta} = \sum_j \frac{m_j}{\rho_j} (v_j^\alpha - v_i^\alpha) \sum_\gamma \frac{\partial W^{ij}}{\partial x_i^\gamma} C^{\gamma\beta}, \quad (13)$$

where the correction tensor $C^{\gamma\beta}$ is the inverse of

$$\sum_j \frac{m_j}{\rho_j} (x_j^\alpha - x_i^\alpha) \frac{\partial W^{ij}}{\partial x_i^\gamma}, \quad (14)$$

that is

$$\sum_j \frac{m_j}{\rho_j} (x_j^\alpha - x_i^\alpha) \sum_\gamma \frac{\partial W^{ij}}{\partial x_i^\gamma} C^{\gamma\beta} = \delta^{\alpha\beta}. \quad (15)$$

This approach leads by construction to first order consistency where the errors due to particle disorder cancel out and the conservation of angular momentum is ensured. Only this allows that rigid rotation can be simulated correctly.

Finally, the sound speed of the material is given by

$$c_s(\rho'_0) = \sqrt{K(\rho'_0)/\rho'_0}. \quad (16)$$

Together with Eq. 9 this relation shows that the soundspeed is a strong function of density. This behaviour has been seen in molecular dynamics simulations by Paszun & Dominik (2008), but there is no data available from laboratory measurements.

Up to this point the set of equations describes a perfectly elastic solid body. Additionally, the material simulated in this work are SiO₂ dust aggregates, which features a high degree of porosity and, thus, plasticity. The modifications accounting for these features are described in the next section.

2.3. Porosity and plasticity

Following the Sirono (2004) model, the porosity Φ is modelled by the density of the porous material ρ and the constant matrix density ρ_s

$$\Phi = 1 - \frac{\rho}{\rho_s} = 1 - \phi, \quad (17)$$

In the following we will use the filling factor $\phi = \rho/\rho_s$.

We model plasticity by reducing inner stresses given by $\sigma^{\alpha\beta}$. For this reason we need constitutive relations describing the behaviour of the material during plastic deformation. These relations are specific for each material and have to be determined empirically. Particularly for highly porous materials it is extremely difficult to acquire them. Therefore, it is an advantageous feature of our model that it is based on measurements by Blum & Schr apler (2004), Blum et al. (2006) and G uttler et al. (2009b).

The main idea of the adopted plasticity model is to reduce inner stress once the material exceeds a certain plasticity criterion. In the elastic case, described by Eqns. 7 and 8, inner stresses grow linearly with deformation. Hence, the material returns to its original shape at vanishing external forces. Reducing inner stresses, i.e. deviating from the elastic deformation path, reduces the internal ability of the material to restore its original shape. Therefore, by stress reduction deformation becomes permanent, i.e. plastic. Following and expanding the approach by Sirono (2004), we treat plasticity for the pure hydrostatic pressure p and the deviatoric stress tensor $S^{\alpha\beta}$ separately.

For the deviatoric stress tensor we follow the approach by Benz & Asphaug (1995) and Sch afer et al. (2007) assuming that our material is isotropic, which makes the von Mises yield criterion applicable. This criterion is characterised by the shear strength Y , which in our model is a composite of the compressive and tensile strengths: $Y(\phi) = \sqrt{\Sigma(\phi)|T(\phi)|}$. The suitability of this choice was already demonstrated in G uttler et al. (2009b). Since $Y(\phi)$ is a scalar we have to derive a scalar quantity from $S^{\alpha\beta}$ for reasons of comparability. We do this by calculating its second irreducible invariant $J_2 = S^{\alpha\beta} S^{\alpha\beta}$. Finally, the reduction of the deviatoric stress is implemented in the following way

$$S^{\alpha\beta} \rightarrow f S^{\alpha\beta}, \quad \text{where } f = \min \left[Y^2(\phi)/3J_2, 1 \right]. \quad (18)$$

The hydrostatic pressure is limited by the tensile strength $T(\phi)$ for $p < 0$ and by the compressive strength $\Sigma(\phi)$ for $p > 0$:

$$p(\phi) = \begin{cases} \Sigma(\phi) & \phi > \phi_c^+ \\ T(\phi) & \phi < \phi_c^- \end{cases}. \quad (19)$$

For $\phi_c^- \leq \phi \leq \phi_c^+$ the material is in the elastic regime and Eq. 8 is applied. ϕ_c^- and ϕ_c^+ denote the filling factors where the elastic path intersects the tensile strength and compressive strength, respectively (see Fig. 1).

The pressure reduction process is implemented such that at any time step p is computed with Eq. 8. If for a given ϕ $p(\phi) > \Sigma(\phi)$ and $\phi > \phi_c^+$ the pressure $p(\phi)$ is reduced to $\Sigma(\phi)$. The deformation becomes irreversible once the new reference density ρ'_0 is computed through Eq. 8 and the elastic path is shifted towards higher densities. Hereby also the limiting filling factors ϕ_c^- and ϕ_c^+ are set anew. In principal there are two possible implementations for this. (1) Plasticity becomes effective immediately and ρ'_0 is computed whenever $p > \Sigma$. (2) Plasticity becomes effective after pressure decrease, which is equivalent to $\phi < \phi_c^+$. We tested both implementations. For our understanding

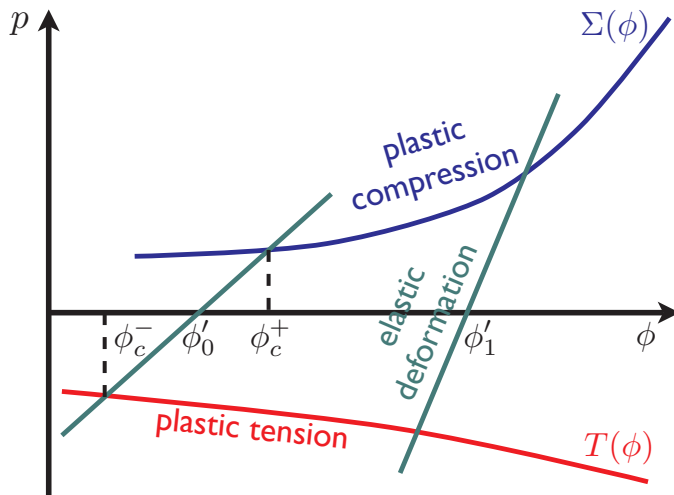


Fig. 1. In the modified Sirono porosity model the regime of elastic deformation is limited by the compressive strength $\Sigma(\phi)$, which represents the transition threshold to plastic compression for $p > \Sigma(\phi)$, and the tensile strength $T(\phi)$, which represents the transition threshold to plastic tension or rupture for $p < T(\phi)$. Returning from one of the plastic regimes to vanishing external pressure via an elastic path leads to a ϕ_1' that differs from the initial ϕ_0' . Hence, the material has been deformed irreversibly.

possibility (1) is closer to the underlying physical process. In addition it proved to be more stable. According to the benchmark parameters the results were equivalent.

For the tensile regime, i.e. for $\phi < \phi_c^-$, we do not adopt the damage and damage restoration model presented in Sirono (2004). This damage model for brittle material such as rocks or pumice has been developed for SPH by Benz & Asphaug (1994, 1995) and was recently used by Jutzi et al. (2008, 2009a,b). It is assumed that a material contains flaws, which are activated and develop under tensile loading (Grady & Kipp 1980). Schäfer et al. (2007) did not find the model applicable in their simulations of porous ice because it includes compressive damage effects. Brittle material like pumice and rocks tend to disintegrate when they are compressed: they crush. Whereas in our material, highly porous SiO_2 dust, tensile and compressive strength increase with compression. This is due to the fact that the monomers are able to form new bonds when they get in contact. Therefore, we adopt the same approach as in the compressive regime and reduce the pressure $p(\phi)$ to $T(\phi)$ once the tensile strength is exceeded. Finally, the material can rupture due to plastic flow. However, material that is plastically stretched can be compressed again up to its full strength. By choosing this approach a “damage restoration model” is implemented in a very natural way.

Finally, a remark has to be made about energy. Apart from energy dissipation by numerical and artificial viscosity we assume intrinsic energy conservation. We suppose that heat production in the investigated physical processes is negligible. Therefore, our model is limited to a velocity regime below the sound speed c_s of the dust material (≈ 30 m/s, see Blum & Wurm 2008; Paszun & Dominik 2008). By choosing the approach of modelling plasticity via stress reduction, we assume that most of the energy is dissipated by plastic deformation, since the reduction of internal stresses accounts for the reduction of internal energy.

Since we do not solve the energy equation thermodynamically enhanced features like any phase transition such as melting and freezing cannot be simulated. This scheme also does not feature a damage model. Especially in the section about fragmentation (Sect. 5.3) the presence of any flaws in the material cannot be taken into account yet, although they might have influence on the resulting fragment distribution.

3. Experimental reference

3.1. Material parameters

The material used for the calibration experiments are highly porous dust aggregates as described by Blum & Schröppler (2004), consisting of spherical SiO_2 spheres with a diameter of $1.5 \mu\text{m}$. For these well defined dust aggregates it is possible to reproducibly measure macroscopic material parameters like tensile strength, compressive strength, and, potentially, also the shear strength as needed for the SPH porosity model (see section 2.3). The tensile strength for this material was measured for highly porous and compacted aggregates ($\phi = 0.15 \dots 0.66$) by Blum & Schröppler (2004). These measurements support a linear dependence between the tensile strength and the number of contacts per monomer (increasing with increasing ϕ), which yields the tensile strength as

$$T(\phi) = - \left(10^{2.8+1.48\phi} \right) \text{ Pa} . \quad (20)$$

The compressive strength was measured in the experimental counterpart of this paper (Güttler et al. 2009b) with an experimental setup to determine the static omni-directional compression (ODC), whereby the sample is enclosed from all sides and the pressure is constant within the sample. We found that the compressive strength curve can be well described by the analytic function

$$\Sigma(\phi) = p_m \cdot \left(\frac{\phi_2 - \phi_1}{\phi_2 - \phi} - 1 \right)^{\Delta \cdot \ln 10} , \quad (21)$$

where the free parameters were measured to be $\phi_1 = 0.12$, $\phi_2 = 0.58$, $\Delta = 0.58$, and $p_m = 13$ kPa. However, these parameters were measured with a static setup and we expect a different strength for a dynamic collision. The parameters ϕ_1 and ϕ_2 determine the range of the volume filling factor, where ϕ_1 is defined by the uncompressed material and ϕ_2 corresponds to the densest packing. These parameters are expected to be the same for the dynamic compression, while p_m and Δ are treated as free parameters, which we will calibrate in the forthcoming sections. The last important material parameter to describe the dust aggregates is the elasticity. We can determine the Young’s modulus from measurement and simulation of the sound speed (Blum & Wurm 2008; Paszun & Dominik 2008), which is $c = 30 \text{ m s}^{-1}$. From this approach the bulk modulus for the uncompressed material is $K_0 = \rho_i c^2 = 300 \text{ kPa}$ with $\rho_i = 300 \text{ kg m}^{-3}$. However, other plausible calculations (Weidling et al. 2009) indicate an elasticity of rather 1 kPa. We will therefore also vary this parameter.

3.2. Calibration experiment

As a setup for an easy and well-defined calibration experiment (see Güttler et al. 2009b), we chose a glass bead with a diameter of 1 to 3 mm, which impacts into the dust aggregate material with a velocity between 0.1 and 1 m s^{-1} under vacuum conditions (pressure 0.1 mbar). We were able to measure the deceleration curve, stopping time, and intrusion depth of the glass bead

(for various velocities and projectile diameters) and the compaction of the dust under the glass bead (for a 1.1 mm projectile with a velocity of 0.65 m s^{-1}). These results will serve for calibrating and testing the SPH code.

For the measurement of the deceleration curve, we used an elongated epoxy projectile instead of the glass bead. The bottom shape and the mass resembled the glass bead, while the lower density and the therefore longer extension made it possible to observe the projectile during the intrusion. The projectile was observed by a high-speed camera (12,000 frames per second) and the position of the upper edge was followed with an accuracy of $\approx 3 \mu\text{m}$. We found that – independently of velocity and projectile diameter – the intrusion curve can be described by a sine curve

$$h(t) = -D \cdot \sin\left(\frac{\pi t}{2 T_s}\right); \quad t \leq T_s. \quad (22)$$

Here, D and T_s denote the intrusion depth and the stopping time of the projectile. The stopping time is defined as the time between the first contact and the deepest intrusion at zero velocity. In Sect. 5.1.2 we will use the normalised form of the intrusion curve with $D = T_s = 1$.

For the intrusion depth we found good agreement with a linear behaviour of

$$D = \left(8.3 \cdot 10^{-4} \frac{\text{m}^2 \text{s}}{\text{kg}}\right) \cdot \frac{mv}{A}, \quad (23)$$

where v is the impact velocity of the projectile and m and $A = \pi r^2$ are the mass and cross-sectional area of the projectile, respectively. We found the stopping time T_s to be independent of the velocity and only depending on the projectile size ($3.0 \pm 0.1 \text{ ms}$ for 1 mm projectiles and $6.2 \pm 0.1 \text{ ms}$ for 3 mm projectiles).

The compaction of dust underneath the impacted glass bead was measured by x-ray micro-tomography. The glass bead diameter and velocity for these experiments correspond to the compaction calibration setup described in Table 1. The dust sample with embedded glass bead was positioned onto a rotatable sample carrier between an x-ray source and the detector. During the rotation around 360° , 400 transmission images were taken, from which we computed a 3D density reconstruction with a spatial resolution of $21 \mu\text{m}$. The according results of the density reconstruction can be found in Güttler et al. (2009b), where we found that roughly one sphere volume under the glass bead is compressed to a volume filling factor of $\phi \approx 0.23$, while the surrounding volume is nearly unaffected with an original volume filling factor of $\phi \approx 0.15$. In this work, we will focus on the vertical density profile through the centre of the sphere and the compressed material (see section 4).

3.3. Further benchmark experiments

In this section, we will present two further experiments which will be used for the validation of the SPH code in sections 5.2 and 5.3. Heißelmann et al. (2007) performed low-velocity collisions ($v = 0.4 \text{ m s}^{-1}$) between cubic-shaped, approx. 5 mm-sized aggregates of the material as described in Sect. 3.1 and found bouncing whereby approx. 95% of the energy was dissipated in a central collision. Detailed investigation of the compaction in these collisions (Weidling et al. 2009) revealed significant compaction of the aggregates (from $\phi = 0.15$ to $\phi = 0.37$) after approx. 1,000 collisions. The energy needed for this compaction is consistent with the energy dissipation as measured by Heißelmann et al. (2007).

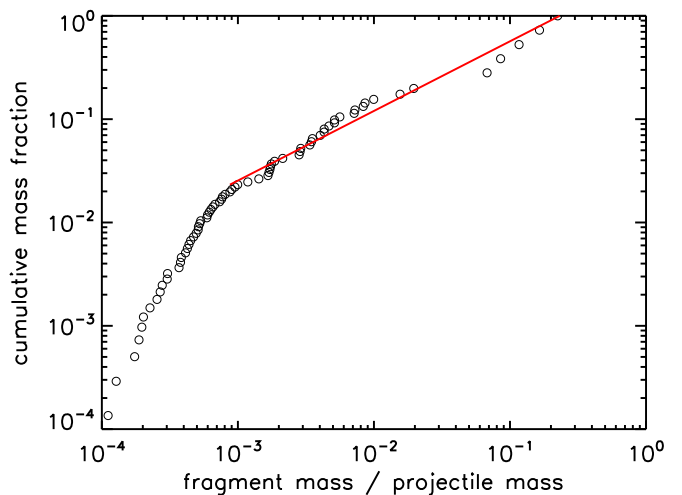


Fig. 2. Cumulative mass distribution of the fragments after a disruptive collision, which can be described by a power law. The divergence for low masses is due to depletion of small aggregates because of the camera resolution.

A further experiment deals with the disruptive fragmentation of dust aggregates (for details see Güttler et al. 2009a,b). In this case, a dust aggregate with a diameter of 0.57 mm consisting of $1.5 \mu\text{m}$ spherical SiO_2 dust with a volume filling factor of $\phi = 0.35$ collides with a solid glass target at a velocity of 8.4 m s^{-1} (also see Fig. 20 in Güttler et al. 2009b). The projectile fragments and the projected sizes of these fragments are measured with a high-speed camera with a resolution of $16 \mu\text{m}$ per pixel. As the mass measurement is restricted to the 2D images, the projected area of each fragment is averaged over a sequence of images where it is clearly separated from others. From this projected area, the fragment masses are calculated with the assumptions of a spheric shape and an unchanged volume filling factor. Fig. 2 shows the mass distribution in a cumulative plot. For the larger masses, which are not depleted due to the finite camera resolution, we find good agreement with a power-law distribution

$$n(m) dm = \left(\frac{m}{\mu}\right)^\alpha dm, \quad (24)$$

where m is the normalised mass (fragment mass divided by projectile mass) and $\mu = 0.22$ is a measure for the strength of fragmentation, being defined as the mass of the largest fragment divided by the mass of the projectile. The exponent α has a value of 0.67. A similar distribution was already described by Blum & Münch (1993) for aggregate-aggregate fragmentation of ZrSiO_4 aggregates with a comparable porosity.

4. Numerical Issues

Before we perform the calibration process, some numerical issues have to be resolved. For instance, it is unfeasible to simulate the dust sample, into which the glass bead is dropping in the compaction calibration experiment presented in section 3, as a whole. It is also unfeasible to carry out all necessary computations in 3D. Therefore, we will only simulate part of the dust sample and explore at which size spurious boundary effects will emerge. Most of the calibration process has been conducted in 2D, but the differences between 2D and 3D results will be discussed and quantified.

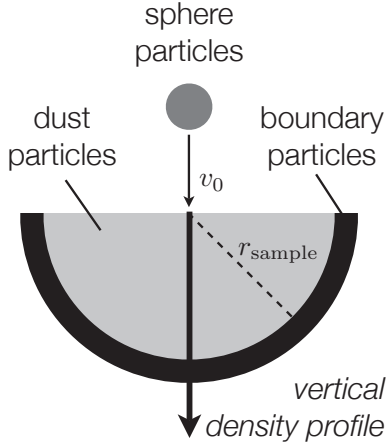


Fig. 3. Compaction calibration setup in 2D or, respectively, cross-section of 3D compaction calibration setup. A glass sphere impacts into a dust sample (radius r_{sample}) with initial velocity v_0 . The dust sample is surrounded by boundary particles at its bottom. Their acceleration is set to zero at every time step. The vertical density profile at maximum intrusion serves as calibration feature.

In this context we make use of 2D simulations in cartesian coordinates although the symmetry of the problem suggests the usage of cylindrical coordinates. However, the SPH scheme in cylindrical or polar coordinates battles with the problem of a singularity at the origin of the kernel function. There exist only few attempts to solve this issue (e.g. Omang et al. 2006), but they are still under development and require high implementation efforts. Since in our case 2D simulations only serve as indicator for calibration and 3D simulations are aimed at, we stick to cartesian coordinates.

The glass bead is simulated with the Murnaghan equation of state

$$p(\rho) = \left(\frac{K_0}{n}\right) \left[\left(\frac{\rho}{\rho_0}\right)^n - 1\right], \quad (25)$$

following the usual laws of continuum mechanics as presented in section 2.2. The compaction calibration setup is initialised with the numerical parameters shown in Table 1, unless stated otherwise in the text. Our tests showed that the maximum intrusion depth and the density profile are the calibration parameters which are most sensitive to changes of the numerical setup. Density profiles (e.g. Figs. 4 and 5) display the filling factor ϕ along a line through the centre of the sphere and perpendicular to the bottom of the dust sample (see Fig. 3). The origin in the diagrams represents the surface of the unprocessed dust sample. The glass sphere has been removed in these figures.

4.1. Computational domain and boundary conditions

In 2D simulations we tested the effect of changing size and shape of the dust sample. Initially the particles were set on a triangular lattice with a lattice constant of $25 \mu\text{m}$. To be geometrically consistent with the cylindrical experimental setup, firstly, we utilised a box (width 8 mm) and varied its depth: 1.375 mm, 2.2 mm, 3.3 mm, and 5.5 mm. This is equivalent to $2.5 \times, 4 \times, 6 \times,$ and $10 \times r_{\text{sphere}}$. Comparing the density profiles (Fig. 4, top), two features are remarkable: (1) The maximum filling factor at the top of the dust sample ($\phi \approx 0.27$ at $D \approx -0.6$ mm) and the intrusion depth D is nearly the same for all dust sample sizes. (2)

Physical Quantity	Symbol	Value	Unit
Glass bead			
Bulk density ^(*)	ρ_0	2540	kg m^{-3}
Bulk modulus ^(*)	K_0	5×10^9	Pa
Murnaghan exponent ^(*)	n	4	-
Radius	r	0.55×10^{-3}	m
Impact velocity	v_0	0.65	m s^{-1}
Dust sample			
Initial density	ρ_i	300	kg m^{-3}
Bulk density	ρ_s	2000	kg m^{-3}
Reference density	ρ'_0	300	kg m^{-3}
Initial filling factor	ϕ_i	0.15	-
Bulk modulus	K_0	3×10^5	Pa
ODC mean pressure	p_m	1300	Pa
ODC max. filling factor	ϕ_2	0.58	-
ODC min. filling factor	ϕ_1	0.12	-
ODC slope	Δ	0.58	-

Table 1. Numerical parameters for the compaction calibration setup. ODC stands for omni-directional compression relation (Eq. 21). Quantities marked by (*) represent the parameters for sandstone in Melosh (1989) which we adopt for glass here.

For $d_{\text{sample}} < 3.3$ mm we find spurious density peaks at the lower boundaries ($D \approx -1.4$ mm and $D \approx -2.2$ mm).

In order to reduce the computation time we simulated the dust sample as a semicircle with the same radius variation as above. The resulting density profiles are shown in Fig. 4 (bottom). In contrast to the corresponding simulations with the box-shaped samples we find for $r_{\text{sample}} \leq 1.375$ mm an increased maximum filling factor and a slightly reduced intrusion depth. Due to the greater amount of volume lateral to the intrusion channel, material can be pushed aside more easily than inside the narrow boundaries of the semicircle. Therefore, a higher fraction of the material is compressed to higher filling factors. For $r_{\text{sample}} > 3.3$ mm the spurious boundary effects become negligible within the compaction calibration setup and the density structure shows no significant difference for box-shaped and semicircle shaped dust samples.

Hence, all computations of section 4 are conducted on the basis of a semicircle in 2D or a hemisphere in 3D with a radius of $r_{\text{sphere}} = 3.3$ mm.

In all cases the dust sample is bordered by a few layers of boundary particles. The acceleration of these particles is set to zero at each integration step, simulating reflecting boundary conditions. Apart from that, i.e. in terms of equation of state, they are treated like dust particles. We also tested damping boundary conditions by simulating two layers of boundaries. The outer layer was treated as described above, the inner (sufficiently large) layer was simulated with a high artificial α -viscosity. Since there was no significant difference in the outcome we fix all boundaries in the afore mentioned way and treat them as reflecting.

4.2. Resolution and Convergence

Jutzi (2008) found in his studies of a basalt sphere impacting into a porous target that the outcome of his simulations strongly depends on the resolution. With a calibration setup similar to the one used in this paper Geretshauer (2006) confirms that also in simulations of the type presented in this work a strong resolution dependence is present. He has found that the intrusion depth of the glass bead can be doubled by doubling the resolu-

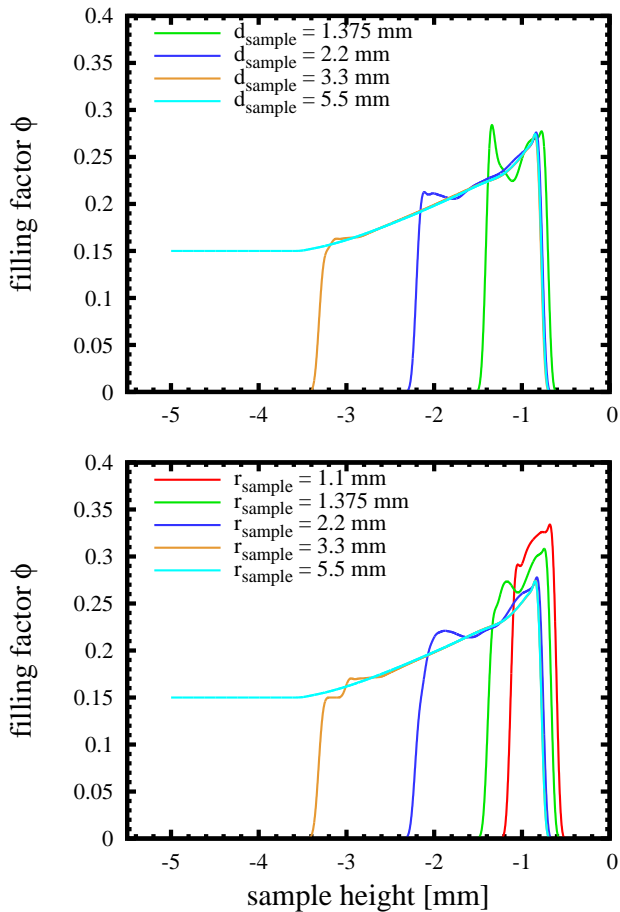


Fig. 4. Vertical density profile at maximum intrusion for the compaction calibration setup and different shapes of the 2D dust sample (box and semicircle). Depth d_{sample} of an 8 mm wide box (top) and radius r_{sample} of the semicircle (bottom) were varied. In both cases spurious boundary effects appear for $d_{\text{sample}} < 3.3$ mm and $r_{\text{sample}} < 3.3$ mm, respectively.

tion. Since the calibration experiments presented in Güttler et al. (2009b) are extremely sensitive even to minor changes of the setup, the convergence properties of porosity model and underlying SPH method will be investigated carefully in this paragraph. Additionally, we will study the differences in the outcome of 2D and 3D setup.

For the 2D convergence study particles were initially put on a triangular lattice again. The lattice constants l_c were 100, 50, 25, and $12.5 \mu\text{m}$ for the compaction calibration setup. The smoothing length h was kept constant relative to l_c at a ratio of $5.6 \times l_c$. The maximum number of interaction partners was $I_{\text{max}} \approx 180$, the average $I_{\text{av}} \approx 100$ and the minimum $I_{\text{min}} \approx 30$.

In the 3D convergence study we are using a cubic lattice with edge lengths $l_c = 100, 50, \text{ and } 25 \mu\text{m}$. The latter was simulated with 3.7 million SPH particles, which represent the limit of our computational resources. We fixed $h = 3.75 \times l_c$ which yielded $I_{\text{max}} \approx 370$, $I_{\text{av}} \approx 240$, and $I_{\text{min}} \approx 70$. The results are presented in Fig. 5. In contrast to the plots in Fig. 4 the glass sphere is not removed here. Coming from the right side of the plot, the filling factor rapidly decreases from a high value outside the scope of the plot indicating the sphere. The filling factor reaches its minimum at an artificial gap between sphere and surface of the dust sample. The width of this gap is about one smoothing length h . The existence of the gap has two reasons: (1) Sphere mate-

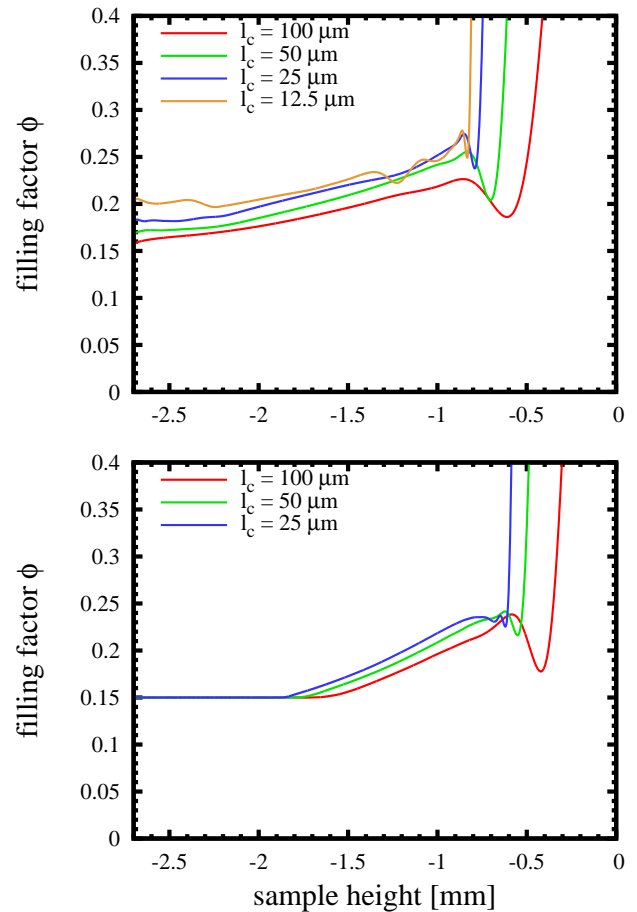


Fig. 5. Convergence study of the vertical density profile for 2D (top) and 3D (bottom) compaction calibration setups. The filling factor increase towards the surface of the dust sample accounts for the glass bead which is not removed in this plot. Simulations were performed for different spatial resolutions. All curves show a characteristic filling factor minimum between sphere and dust sample and a characteristic filling factor maximum indicating the dust sample surface.

rial and dust material have to be separated by artificial viscosity due to stability reasons. This will be discussed below. (2) The volume of the sphere represents an area of extremely high density and pressure with respect to the dust sample. This area is smoothed out due to the SPH method. The width of the smoothing is given by the smoothing length. Although a clear convergence behaviour is visible in Fig. 5 for both the 2D and the 3D case, a more unique convergence criterion has to be found. For this purpose we choose the maximum intrusion depth which proved to be very sensitive to resolution changes. The shape of the filling factor profile offers two choices to determine the intrusion depth: (1) The filling factor minimum which represents the middle between sphere and dust sample and (2) the filling factor maximum (peak) of the dust material left to the gap between sphere and dust sample.

Fig. 6 shows the results for both cases in 2D (top) and 3D (bottom). The error bars around the minimum values represent the smoothing length and give an indication of the maximum error. The position of the density peak remains almost constant, converging to ≈ -0.9 mm (2D) and ≈ -0.65 mm (3D), respectively, for higher resolutions. The position of the density minimum at low resolutions significantly differs from the position

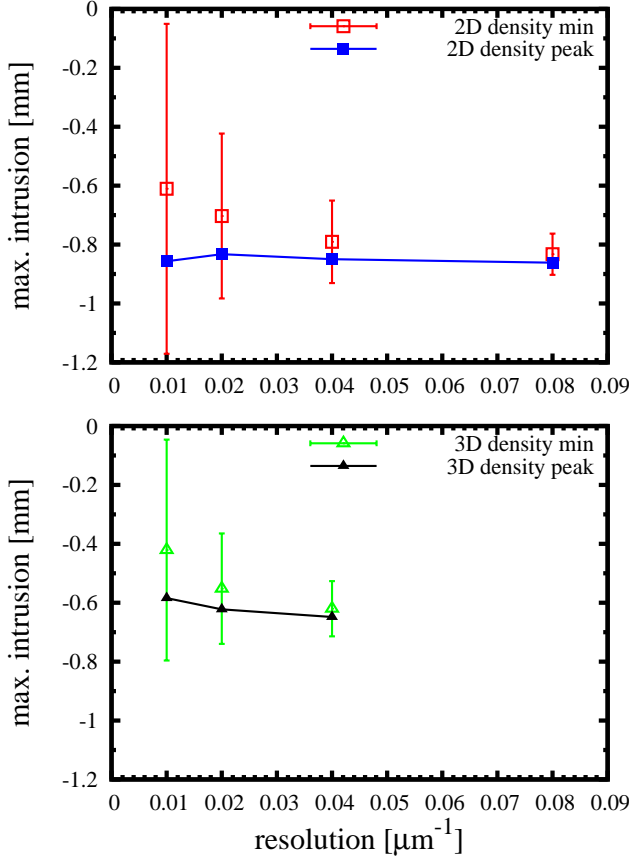


Fig. 6. Convergence study of the maximum intrusion depth for the 2D (top) and 3D (bottom) compaction calibration setups. Filled symbols represent the position of the filling factor peak of the dust material, whereas empty symbols denote the position of the minimum filling factor at the gap between glass bead and dust material. The values are derived from the density profiles in Fig. 5. The smoothing length is indicated by the error bars. While the peak position remains almost constant at ≈ -0.9 mm (2D) and ≈ -0.65 mm (3D) with increasing spatial resolution, the position of the filling factor minimum quickly converges to the same value. This is due to the artificial separation of dust and glass materials, which is in the order of a smoothing length.

of the density peak, but converges quickly to the same intrusion depth with higher resolutions. However, the differences between the extrema remain well within one smoothing length. This is due to the fact that sphere and dust sample are separated by about one smoothing length. Comparing 2D and 3D convergence the 3D case seems to converge more quickly.

Due to the findings of this study we choose a spatial resolution of $l_c = 25 \mu\text{m}$ for further simulations in 2D. In the 3D case $l_c = 50 \mu\text{m}$ is sufficient, but $l_c \leq 50 \mu\text{m}$ is desirable if it is feasible. After defining suitable values for the spatial resolution we now turn to the numerical resolution, which for the SPH scheme is given by the number of interaction partners of each single particle. For the investigation of this feature we performed a study utilising the 2D compaction calibration setup with a spatial resolution of $l_c = 25 \mu\text{m}$ and varied the ratio between smoothing length and lattice constant h/l_c from 2 to 7 in steps of one. h/l_c determines the initial number of interaction partners that is smoothed over. The resulting maximum, average, and minimum interactions I_{max} , I_{av} , and I_{min} and the corresponding smoothing

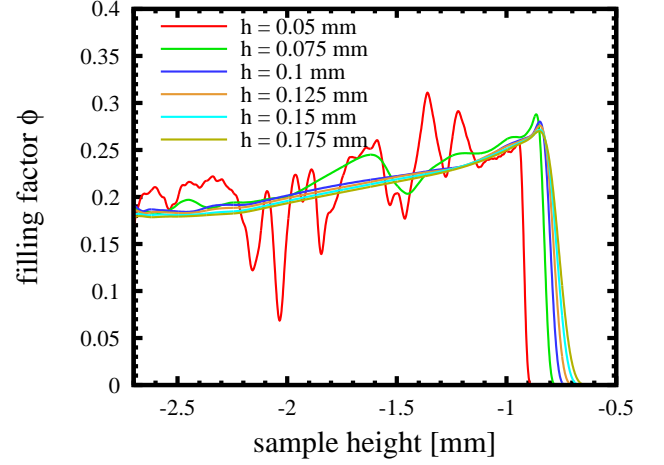


Fig. 7. Convergence study for the density profile using the 2D setup and varying the smoothing length h . Through this variation the number of interaction partners is varied according to Table 2. The glass bead has been removed in this plot. For $h \leq 0.075$ mm clear signs of instabilities are visible. For $h \geq 0.1$ mm the filling factor has the same value and its position remains constant. The smoothing of the boundary of the dust sample is increased for increasing h .

Table 2. Parameters for the convergence study regarding interaction numbers

h	h/l_c	I_{min}	I_{av}	I_{max}	T_{comp}	N_{steps}
0.050 mm	2	3	13	25	16.2 h	132401
0.075 mm	3	10	30	55	14.8 h	96912
0.100 mm	4	16	53	92	19.8 h	71175
0.125 mm	5	23	82	142	19.0 h	56347
0.150 mm	6	32	116	205	21.6 h	46782
0.175 mm	7	43	158	274	24.3 h	39980

lengths h can be found in Table 2. Additionally, we measured the computation time T_{comp} that the simulations took on 4 cores of a cluster with Intel Xenon Quad-Core processors (2.66 GHz) for a simulated time of 5 ms and the number of integration steps N_{step} of our adaptive Runge-Kutta Cash-Karp integrator.

Comparing the density profiles in Fig. 7 (where the glass bead has been removed) instabilities in the form of filling factor fluctuations due to insufficient interaction numbers appear for smoothing lengths $h \leq 0.075$ mm, i.e. for $I_{\text{av}} \leq 30$. For $h \geq 0.1$ mm the density profile maintains essentially the same shape: The position and height of the filling factor peak remains nearly the same and ϕ smoothly drops to ≈ 0.18 towards the bottom of the dust sample. Only the sharp edge at the top of the dust sample is smoothed out over a wider range due to the increased smoothing length.

Table 2 shows that the number of integration steps N_{step} is decreasing with increasing interaction numbers. This is due to the fact that elastic waves inside the dust sample are smoothed out over a wider range causing the adaptive integrator to increase the duration of a time step, since density fluctuations do not have to be resolved as sharply as at smaller smoothing. As expected, the computation time T_{comp} is generally increasing with increasing number of interactions. There are two exceptions: $h = 0.075$ mm and $h = 0.125$ mm. Here, the decrease of N_{steps} overcompensates the increase of interactions leading to a decrease of T_{comp} . Hence, a ratio $h/l_c \approx 5$ yields the necessary accuracy and an ac-

ceptable amount of computation time. This study also justifies the choice of $h/l_c = 5.6$ in Güttler et al. (2009b) and we will stick to this ratio throughout this paper.

According to these findings, for 3D simulations theoretically an average interaction number of $I_{av}^{3/2} \approx 750$ would be needed to achieve the same numerical resolution. However, alike simulations are unfeasible and our choice of $I_{av} \approx 240$ in 3D is equivalent to $I_{av} \approx 40$ in 2D which should provide sufficient and reliable accuracy.

4.3. Geometrical difference – 2D and 3D setups

As one can easily see in Fig. 6 2D and 3D simulations have significantly different convergence values for the intrusion depth. This deviation is caused by the geometrical difference of the 2D and 3D setup. The 2D setup (glass circle impacts into dust semi-circle) represents a slice through a glass cylinder and a semi-cylindrical dust sample, which implies an infinite expansion into the third spatial direction. Whereas the 3D setup represents a real sphere dropping into a “bowl” of dust. The relation for the intrusion depth found by Güttler et al. (2009b) (see Sect. 3) contains a geometrical dependence: $D \propto mv/A$, where D is the intrusion depth, m the mass of the impacting glass bead, v its impact velocity, and A its cross-section. m_{2D} is a mass per unit length. Güttler et al. (2009b) already exploited this relation in order to determine a rough correction factor between 2D and 3D simualtional setups:

$$\frac{m_{3D}v}{A_{3D}} = \frac{\frac{4}{3}\pi r^3 \rho \cdot v}{\pi r^2} = \frac{8}{3\pi} \frac{\pi r^2 \rho \cdot v}{2r} = \frac{8}{3\pi} \frac{m_{2D}v}{A_{2D}}. \quad (26)$$

Hence, the 2D intrusion depth has to be corrected by a factor of $\approx \frac{8}{3\pi}$ in order to determine the 3D intrusion depth. The comparison is shown in Fig. 8. Again we choose the 2D and 3D data gained in the convergence study for the peak filling factor values shown in Fig. 6. Fig. 8 shows the original 2D data, the corrected 2D data, and the according 3D data (with error bars displaying the smoothing length). The 3D values nicely follow the rough correction and remain well within the maximum error. This comparison justifies the correction of the results in Güttler et al. (2009b). With the aid of this – now verified – correction factor the 2D data of the intrusion depth can be converted into 3D data and all calibration tests involving the intrusion depth can be carried out in 2D, which saves a significant amount of computation time. Comparing the vertical density profiles of 2D and 3D setups in Fig. 5 resolves also another issue that remained unsolved in Güttler et al. (2009b). According to the experimental data the filling factor drops to a value of $\phi \approx 0.16$ within ≈ 0.6 mm away from the bottom point of the glass bead. For high-resolution 2D simulations (Fig. 5, top) the filling factor does not drop to this value within the whole dust sample. However, the 3D simulations (Fig. 5, bottom) show that this effect again is due to the difference of 2D and 3D geometry. With the 3D setup the filling factor drops to $\phi \approx 0.16$ within ≈ 0.9 mm. All deviations from experimental findings due to this effect, in particular the presence of a large amount of volume with $\phi \leq 0.2$ in the cumulated volume over filling factor diagram (Fig. 15 in Güttler et al. 2009b), can in principal be removed by switching to 3D simulations. They do not represent a fundamental error in the porosity model.

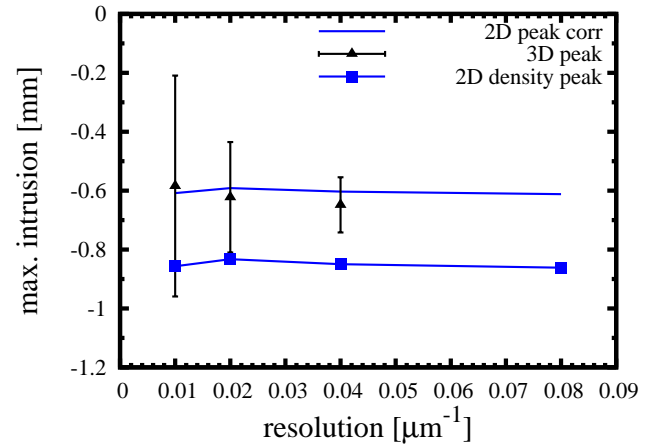


Fig. 8. Verification of the 2D-3D correction factor. Filled symbols denote the position of the filling factor peak of the dust material in Fig. 5. Triangles represent 3D and squares 2D values. The conversion from 2D to 3D intrusion depth utilising the correction factor from Eq. 26 and Eq. 23 due to the geometrical difference is indicated by the line without symbols. The 3D values are in very good agreement with the very rough theoretical prediction. They lie well within the errors.

4.4. Artificial Viscosity

Since artificial viscosity plays an eminent role for the stability of SPH simulations we investigate its influence on the outcome of our compaction calibration setup. Only artificial α -viscosity is applied in our test case, but in a threefold way: (1) It damps high oscillation modes of the glass bead caused by the stiff Murnaghan equation of state (EOS). Thereby it enlarges the time step of our adaptive integrator and saves computation time. (2) It is used to provide the dust material with a basic stability. (3) It separates the areas of Murnaghan EOS and dust EOS and prevents a so called “cannonball instability”. For all three cases also the influence of β -artificial viscosity has been tested, but its influence on all benchmark parameters was negligible.

(1) The choice of the α -viscosity of the *glass bead* proved to be very uncritical. We choose the canonical value $\alpha = 1.0$. There was no influence on the physical benchmark parameters for all α values, except $\alpha = 0$ which produces an instability. Values for $\alpha > 1.0$ show no significant effect on the damping and the influence of $0.1 < \alpha < 1.0$ on it is not too high, but still observable. Hence, we stick to the canonical value.

(2) Sirono (2004) applies no artificial viscosity to his porous ice material because of its spurious dissipative properties. Our findings, shown in Fig. 9, confirm this assessment regarding the *dust material*. Within our 2D compaction calibration setup ($l_c = 25 \mu\text{m}$, $h/l_c = 5.6$) we vary α from 0 to 2 and observe its influence on the density profile (Fig. 9, top) and the maximum intrusion represented by the filling factor peak of the dust material (Fig. 9, bottom).

The position of the filling factor peak ranges from ≈ -0.92 mm with $\alpha = 0.0$ to ≈ -0.62 mm at $\alpha = 2.0$. This clearly demonstrates the dissipative feature of the α -viscosity, since a smaller amount of kinetic energy of the glass bead is transformed into plastic deformation with higher α . The residual energy must have been dissipated. However, the α -viscosity-intrusion curve seems to saturate at a value of ≈ -0.6 mm. The decrease of the maximum intrusion can also be seen in the density profile (Fig. 9, top). While the profile maintains nearly the same shape,

the height of the filling factor peak is decreasing with increasing α . Hence, an increasing artificial viscosity diminishes the peak pressure during compaction, which is via the compressive strength relation $\Sigma(\phi)$ directly responsible for the height of the filling factor peak.

In contrast to Sirono (2004) we find it necessary to apply a small amount of α -viscosity to the dust material. For $\alpha < 0.1$ the results show traces of an instability, which is also responsible for a rapid increase of the maximum intrusion. Therefore, we find it convenient to apply an artificial viscosity with $\alpha = 0.1$ to the dust material, which holds for the previous simulations of this section as well as the following. The choice of a non-zero α , however, is also justified by experimental findings: After impacting into the dust sample the glass bead shortly oscillates due to the elastic properties of the dust. This oscillation is damped by internal friction, which we model with artificial viscosity. Therefore, by choosing a non-zero α we take into account the dissipative properties that our dust material naturally has. A quantitative calibration of this parameter, however, has to be left to future work.

(3) During our first simulations with the 2D compaction calibration setup we observed what is sometimes described in the literature as “cannonball instability”: During the compaction process, when the glass bead intrudes into the dust material, single particles at the sphere’s surface start to oscillate between the domains of the Murnaghan EOS and dust EOS. Due to the severe discrepancy of the “stiffness” of these two equations of state the particles collect a huge amount of kinetic energy until they are fast enough to generate a pressure on the dust material that exceeds the compressive strength $\Sigma(\phi)$. Eventually they disengage from the sphere’s surface like a cannonball and dig themselves into the dust sample causing a huge amount of unphysical compaction. We tackle this problem by applying to all SPH particles with dust EOS, which interact with glass bead SPH particles, the same amount of α -viscosity as to the sphere, i.e. $\alpha = 1.0$. In our simulations this is sufficient to prevent the “cannonball instability”. The spurious dissipation caused by this measure is negligible.

5. Calibration

5.1. Compressive Strength - Compaction Properties

In this section we will refine and extend a study of the compaction properties of the dust sample, which was already carried out in a similar, but less detailed way in Güttler et al. (2009b). There it turned out that the quantity having the most influence on the compaction was the compressive strength relation $\Sigma(\phi)$ (Eq. 21), which was measured in an omni-directional and static manner. In order to adopt this relation for dynamic compression the mean pressure p_m and the “slope” of the Fermi-shaped curve Δ can be treated as free parameters. The upper and lower boundaries of the filling factor ϕ_2 and ϕ_1 , respectively, remain constant even in the dynamic case. Güttler et al. (2009b) found that by lowering p_m most of the features of the compaction calibration setup can be reproduced in a very satisfactory manner. Hereby the filling factor over compressive strength curve (see also Fig. 2 in Güttler et al. 2009b) is shifted towards lower pressures and the yield pressure for compression is lowered. Using only 2D simulations and a rough parameter grid Güttler et al. (2009b) fix $p_m = 1.3$ kPa. The “slope” Δ has not been considered. In this work we will consider Δ and we will perform more accurate parameter studies for p_m . From the latter we will predict a reasonable choice for p_m , which will represent the basis for a 3D simulation of the compaction calibration setup. The results of

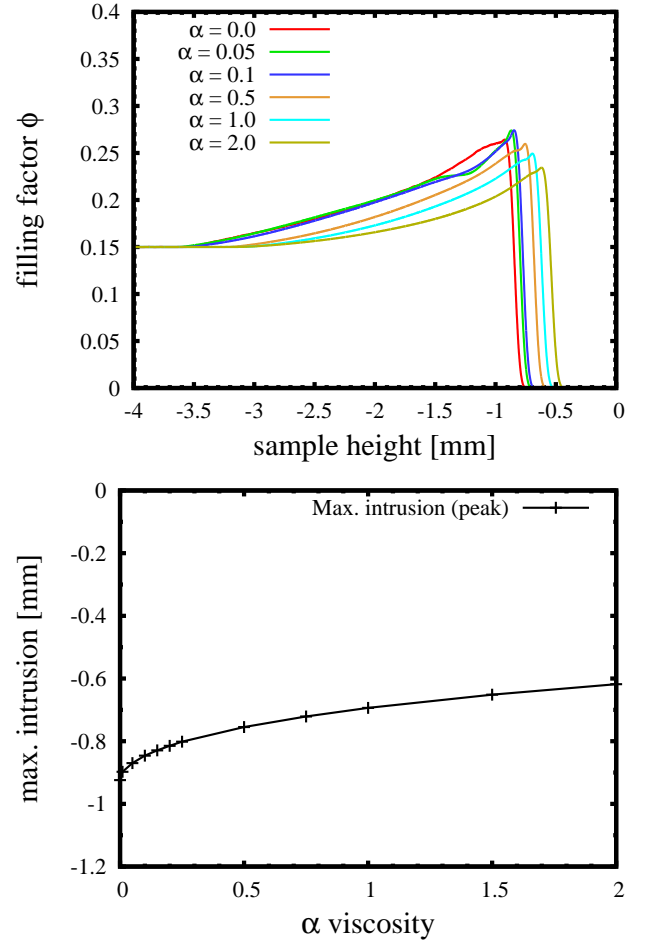


Fig. 9. Density profile (top) and maximum intrusion (bottom) for different values of artificial α -viscosity. The shape of the density profile hardly changes, but increasing α -viscosity decreases the maximum filling factor and the maximum intrusion depth.

this simulation will be compared to results from the laboratory. For the comparison we use the same features as Güttler et al. (2009b).

5.1.1. Fixing free parameters

Since there are no empirical data available for p_m in the dynamical compressive strength curve we perform a parameter study in order to determine a suitable choice for this important quantity. For this study we make use of the 2D compaction calibration setup and vary p_m from 0.13 to 13.0 kPa (Fig. 10 and 11), where 13.0 kPa represents the value for the static compressive strength curve. The effect of lowering p_m can most clearly be seen in the vertical filling factor profile (Fig. 10, top). First of all, more material can be compressed and it is compressed to higher filling factors. As a consequence the glass bead intrudes deeper into the dust sample. From experimental results we expect an intrusion depth of about one sphere diameter (≈ 1 mm). With the aid of the empirical relation between momentum over impactor cross-section mvA^{-1} and intrusion depth D (Eq. 23) as well as the correction factor between 2D and 3D intrusion depth (Eq. 26) we estimate that $D^{3D} \approx 1$ mm corresponds to $D^{2D} \approx 1.42$ mm. Fig. 11 shows the maximum intrusion over the stopping time for various values of p_m (labels). The estimated D^{2D} is indicated by a

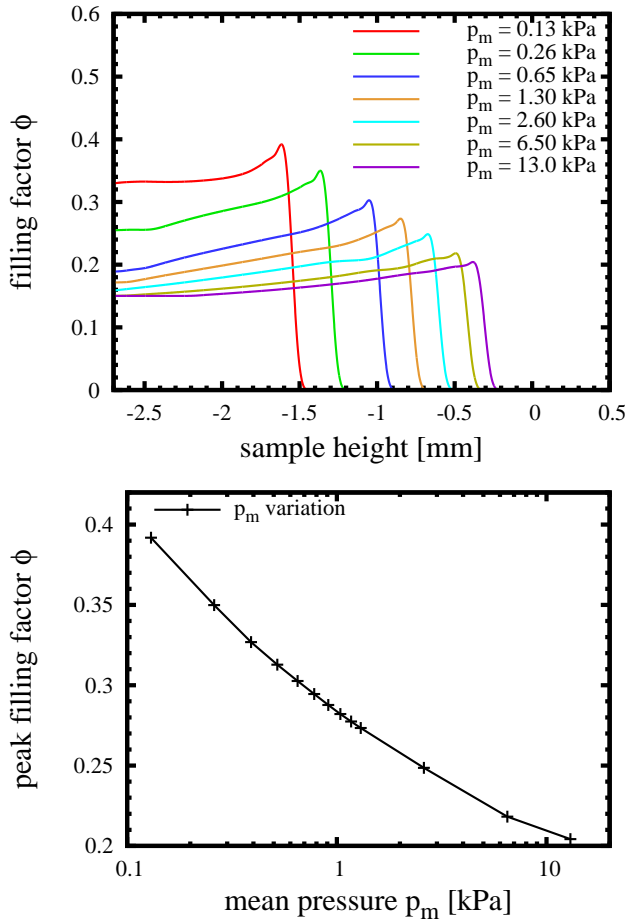


Fig. 10. Density profile (top) and maximum peak filling factor from the density profile over p_m (bottom) for different values of p_m , which represents the mean pressure in the compressive strength relation $\Sigma(\phi)$ (Eq. 21). Lowering p_m from 13.0 kPa (static compressive strength) increases the compressed volume, its filling factor, and the maximum intrusion depth of the glass bead. The parameter study has been performed using the 2D compaction calibration setup.

dashed line. We deduce that regarding intrusion depth a dynamic mean pressure $p_m = 0.26$ kPa is a suitable choice.

This is supported by the peak filling factor appearing in the filling factor profile (Fig. 10, bottom). Empirical data indicate that in case of the compaction calibration setup a peak filling factor $\phi_{\max} \approx 0.3$ can be expected. The comparison between 2D and 3D results (Sect. 4.3) has shown that the peak filling factor in the vertical density profile in the 2D case is generally higher than for the same situation in 3D. The equivalent of $\phi_{\max}^{3D} \approx 0.3$ is a maximum filling factor of $\phi_{\max}^{2D} \approx 0.34$ in 2D. This points to a choice of $p_m \approx 0.3$ kPa, which is consistent with the findings from the intrusion depth.

The compressive strength relation $\Sigma(\phi)$ (Eq. 21) contains a second free parameter Δ , which accounts for the “slope” of the Fermi-shaped curve. In Gütler et al. (2009b) this parameter was chosen to be the same as the one of the static omni-directional compressive strength curve and a closer investigation was not carried out. In order to understand its effect on the compaction properties of the dust sample we are utilising the 2D compaction calibration setup again and vary Δ from 0.55 to 0.80. The results are presented in Fig. 12. From the vertical density profile (Fig.

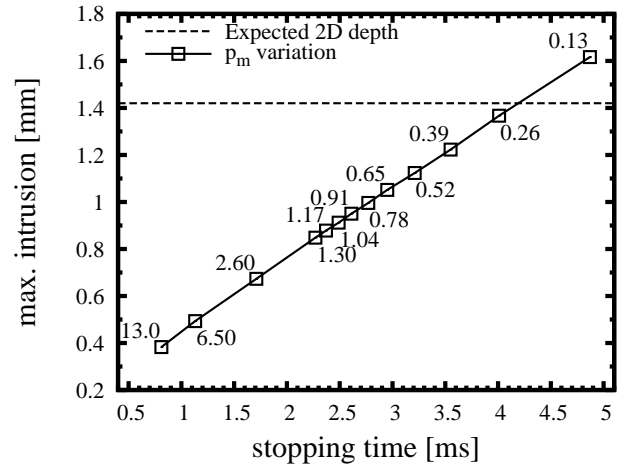


Fig. 11. Maximum intrusion over stopping time for different values of the mean pressure p_m (labels, in kPa) in the compressive strength relation $\Sigma(\phi)$ (Eq. 21) using the 2D compaction calibration setup. The dashed line indicates the 2D intrusion depth that is equivalent to a 3D intrusion depth of ≈ 1 mm according to Eq. 23 and the 2D-3D correction factor from Eq. 26. This supports the choice of the mean pressure $p_m = 0.26$ kPa for further simulations.

12, top) it can be seen that increasing Δ increases the intrusion depth, but not as effectively as by lowering the mean pressure p_m . This is due to the fact that increasing Δ is hardly increasing the peak filling factor in the vertical density profile. More volume is compacted to lower filling factors. Whereas by lowering p_m the total amount of volume that is compacted is smaller, but it is compacted to higher filling factors. This behaviour can be seen comparing the density profiles for the p_m variation (Fig. 10, top) and Δ variation (Fig. 12, top) and particularly from the cumulated volume over filling factor curve (Fig. 12, bottom). This figure shows the normalised fraction of compacted volume corresponding to a volume filling factor $> \phi$. The intersection of the curves with the y-axis represents the total compressed volume, which is increased from ≈ 7 to ≈ 9.5 sphere volumes. According experimental measurements here expect a value of roughly one sphere volume (see section 3.2). Especially for $0.18 < \phi < 0.23$ the compacted volume fraction is increased. The equivalent figure for the p_m variation can be found in Gütler et al. (2009b, Fig. 15). From the comparison of 2D and 3D calibration setups (section 4.3) we know that a huge amount of this compaction (especially in the lower filling factor regime) is due to the geometrical difference. However, the experimental data do not indicate a particularly high amount of compaction to lower filling factors (rather the contrary) and, therefore, we maintain our initial choice of $\Delta = 0.58$.

5.1.2. Comparison with experiments

For the comparison with experiments we performed a simulation using the 3D compaction calibration setup (see Table 1) with two exceptions: (1) The bulk modulus of the dust material was set to $K_0 = 2$ kPa (instead of $K_0 = 300$ kPa) since findings presented below indicated a much lower bulk modulus. However, the choice of K_0 has little influence on the compaction properties calibrated for in the compaction calibration setup. It is more important for bouncing and fragmentation, which will be shown below. (2) The mean pressure of the compressive strength re-

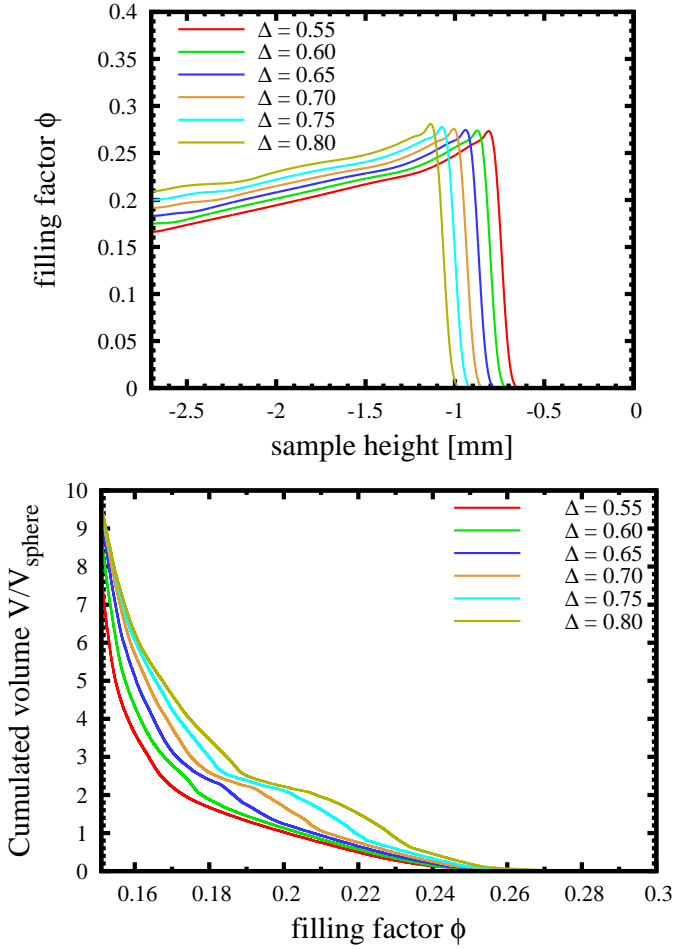


Fig. 12. Density profile (top) and normalised volume fraction of compacted volume over its corresponding filling factor (bottom) for different values of Δ in the compressive strength relation (Eq. 21). Increasing Δ increases the amount of compacted volume at filling factors $0.18 < \phi < 0.23$ and thereby the maximum intrusion depth. Whereas the peak filling factor in the density profile is not changed.

lation (Eq. 21) was set to $p_m = 0.26$ kPa as suggested in the previous section.

The following features of the compaction calibration setup were measured in the laboratory and will be used here for comparison: (1) the stopping time T_s , (2) the intrusion curve of the projectile, (3) the vertical density profile, (4) the cumulated volume over filling factor curve, and (5) the cross-section through sphere and dust sample displaying the filling factor.

(1) The experiments show that the stopping time T_s of the glass bead, i.e. the time from first contact with the dust sample until deepest intrusion, is nearly constant at $T_s^{\text{exp}} = 3.0 \pm 0.1$ ms for 1 mm projectiles over different impact velocities (see section 3.1). In our simulation we find $T_s^{\text{sim}} = 2.42 \pm 0.05$ ms, which is not in excellent agreement but also not too far off the experimental results.

(2) The intrusion curve $h(t)$ was cleared from gravity effects and normalised through $h'(t') = h(t)/D$ and $t' = t/T_s$, where $h(t)$ is the position of the bottom of the glass bead as a function of time, D the maximum intrusion depth, and T_s the stopping time. At first contact t is $h'(t' = 0) = 0$ and at deepest intrusion $h'(t' = 1) = -1$ (see also Güttler et al. 2009b, section 3.2.2). The comparison is shown in Fig. 13: The intrusion curve generated

by our simulation lies well within the data from the experiments with 1 mm and 3 mm spheres and only slightly below the sine curve fitted to the empirical data.

(3) The comparison between the experimentally measured vertical density profile and the result from our simulation is shown in Fig. 14. The crosses represent the data from two experiments where the sphere has not been removed for the measurement. For this reason the filling factor reaches extremely high values at ≈ -1 mm indicating the bottom of the glass bead. The vertical density profile of our simulation is given by the solid line and the vertical dashed line is placed at its filling factor peak at -1.02 mm representing the maximum intrusion depth. Comparing with the experimentally measured maximum intrusion depth of -1.07 mm this is an excellent result. Since a depth of ≈ -1 mm was aimed for using Eqns. 23 and 26 and the 2D intrusion depth study of the previous section this result also supports the validity of these relations. In addition to the exact value of the intrusion depth our simulation also reproduces the shape of the given experimental vertical density profile very well. Only the step-like structure at ≈ -1.5 mm does not find an equivalent in our simulation but it is nicely interpolated.

(4) The vertical density profile shows only a cut through the compressed volume. It contains information about the exact structure of the compression. The cumulated volume over filling factor curve (Fig. 15) has the advantage that it represents the total compressed volume together with its filling factors, hence, these features are not fully independent but focus on different aspects of the compression. The cumulated volume is normalised through the sphere volume. It accounts for the volume fraction of compacted area corresponding to a volume filling factor $> \phi$. In general, the experimental reference and our simulation show a very good agreement. Slightly too much volume is compressed to high filling factors in the simulation which leads to an almost constant deviation for $\phi < 0.26$. However, the slope is reproduced very well.

(5) The comparison between the cross-sections through sphere and dust sample along the z -axis (Fig. 16) reveals reasons for the excess of compressed volume. First, the cross-section of the sphere is artificially enhanced by the smoothing of its boundaries, which is inherent of the SPH method. One effect of the smoothing is the existence of a gap between sphere and dust sample, which was already discussed in Sect. 4.2 and is also clearly visible in Fig. 16 (top). Hence, we assume that the dust sample actually begins, where it has its maximum compression. The fact that the sphere pokes out of the dust sample a bit more than in the experiment has its reason also in the artificial enlargement of the cross-section. Second, it can be seen that in the experimental reference (Fig. 16, bottom) the compacted region is much narrower and more concentrated underneath the sphere. In the simulated result the compacted region is a bit broader. This indicates that the shear strength seems to be a bit smaller than we assume. Third, the compaction reaches too high filling factors, which was already visible in the cumulated volume diagram. Nevertheless, both cross-sections match very well, especially with respect to the mediocre resolution. Remarkably, even the slight intrusion channel on the left and right side of the sphere, which features a slight compression, can be reproduced.

5.2. Bulk Modulus

As it was mentioned in section 3.1 there are two estimates for the bulk modulus K_0 for the uncompressed material with $\phi \approx 0.15$. K_0 in our model is also the pre-factor for computing the bulk modulus for higher filling factors with the aid of

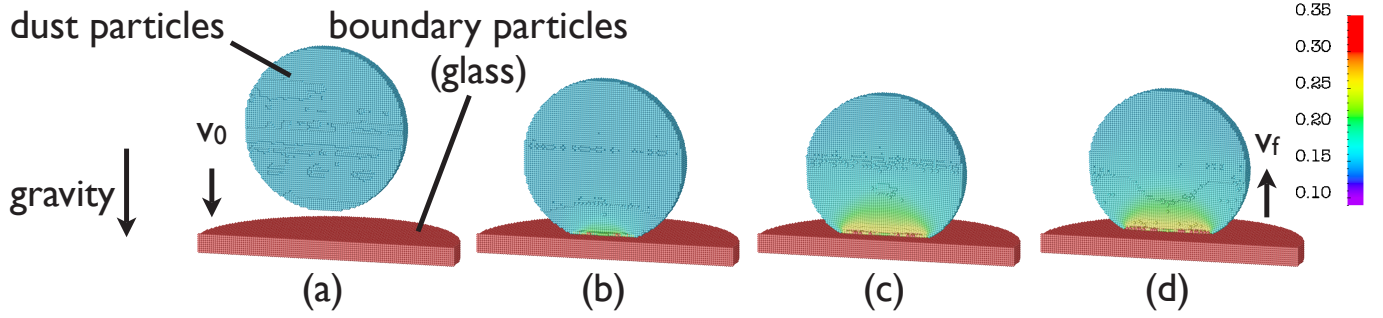


Fig. 17. Bouncing sequence for $t = 0$ ms (a), $t = 10$ ms (b), $t = 18$ ms (c), and $t = 25$ ms (d). The colour code indicates the filling factor. An aggregate consisting of dust particles (Sirono EOS, diameter 1.0 mm) hits a solid surface simulated by boundary glass particles (Murnaghan EOS, diameter 1.6 mm, thickness 0.1 mm) with a velocity of $v_0 = 0.2 \text{ m s}^{-1}$. For this simulation a bulk modulus of $K_0 = 5.0 \text{ kPa}$ and $p_m = 0.26 \text{ kPa}$ were used. The aggregate hits the surface and starts to be compacted at its bottom (b). While the plastic deformation at the bottom increases, the aggregate is also deformed elastically: it gets broader (c). Eventually it leaves the surface with a final velocity v_f (d). It features a permanent compaction, while the elastic deformation vanishes. (An animation of this figure is available in the online journal.)

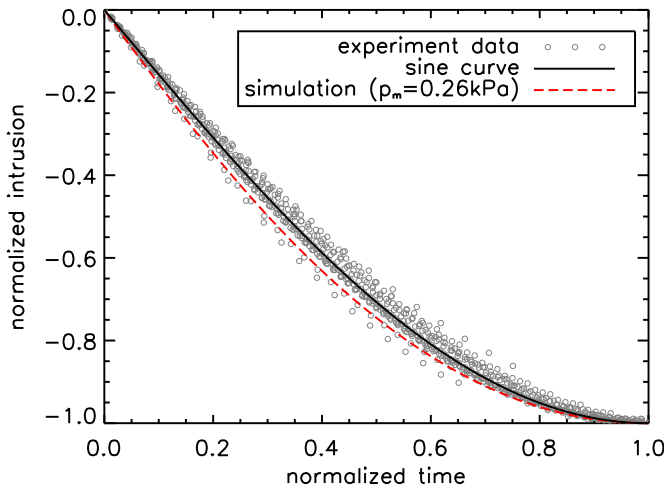


Fig. 13. Comparison between intrusion curves from drop experiments using 1 mm and 3 mm spheres and our 3D simulation (mean pressure $p_m = 0.26 \text{ kPa}$). The curves are normalised such that the origin represents first touch of sphere and dust sample and (1,-1) denotes stopping time at maximum intrusion. The simulated curve lies slightly underneath the fit to the experimental data, but well within the errors. The deviation is due to a smaller stopping time than in the experiments.

a power law (Eq. 9). Since these indirect findings, 1 kPa (see Weidling et al. 2009) and 300 kPa (from sound speed measured by Blum & Wurm 2008; Paszun & Dominik 2008), differ by two orders of magnitude, we try to find a suitable value for K_0 utilising a calibration experiment.

Simulating the low velocity collision setup by Weidling et al. (2009), a 3D dust sphere ($\phi_i = 0.15$, 1 mm diameter, 267737 particles, $l_c = 12.5 \mu\text{m}$) drops onto a solid surface (cylindrical, 1.6 mm diameter, 0.1 mm thick, 115677 particles, $l_c = 12.5 \mu\text{m}$) with initial velocity $v_0 = 0.2 \text{ m s}^{-1}$ (see Fig. 17). The material parameters are shown in Table 3. The bulk modulus K_0 is varied with respect to two values of the mean pressure p_m in the compressive strength relation (0.26 kPa and 1.3 kPa). During the impact a small region of the bottom of the dust sphere is compacted. Then the deformed sphere bounces off the target with

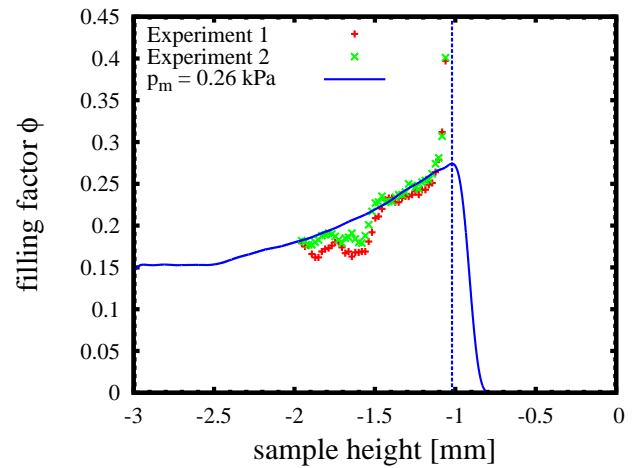


Fig. 14. Comparison between experimentally measured (crosses, sphere not removed) and simulated (solid line, sphere removed) density profiles at maximum intrusion for the compaction calibration setup. The dashed line indicates the position of the simulated maximum intrusion depth given by the density peak at -1.02 mm . The simulation was carried out in 3D using a mean pressure $p_m = 0.26 \text{ kPa}$ for the compressive strength relation (Eq. 21). Both profiles are in excellent agreement. The fact that the step-like structure of the experimental data cannot be seen in the simulation is a minor drawback since it is interpolated nicely.

reduced velocity v_f (see Fig. 17). The latter effect was already observed in Güttler et al. (2009b) and demonstrates the ability of our code and the implemented porosity model to simulate the elastic properties of the dust correctly. In this study we have doubled the resolution and determine the coefficient of restitution $\varepsilon_{\text{rest}} = v_f v_0^{-1}$ depending on K_0 (see Fig. 18).

The bouncing calibration setup is equivalent with two centrally colliding dust aggregates at 0.4 m s^{-1} , thus, our results are comparable to Heißelmann et al. (2007): $\varepsilon_{\text{rest}} \approx 0.2$ and $\approx 95\%$ energy dissipation.

Based on the results of the previous section, where $p_m = 0.26 \text{ kPa}$ turned out to be a good choice for the mean pressure, our results of this experiment favour a bulk modulus $K_0 \approx 5 \text{ kPa}$. This value is close to $K_0 = 1 \text{ kPa}$ computed by Weidling et al.

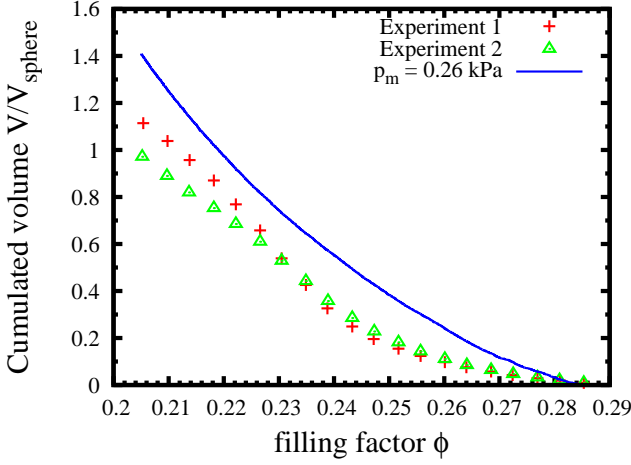


Fig. 15. Total cumulated volume over filling factor for drop experiments (crosses and triangles) and our 3D simulation with mean pressure $p_m = 0.26$ kPa (solid line). The plot shows the cumulated mass fraction (normalised through the sphere volume) with a filling factor $> \phi$ over ϕ . Our simulation is in good agreement with the experimental findings. However, a higher amount of volume compressed to high filling factors leads to an almost constant deviation for $\phi < 0.26$. The slope is reproduced very well.

Physical Quantity	Symbol	Value	Unit
Glass plate			
Bulk density ^(*)	ρ_0	2540	kg m ⁻³
Bulk modulus ^(*)	K_0	5×10^9	Pa
Murnaghan exponent ^(*)	n	4	-
Radius	r_{plate}	0.8×10^{-3}	m
Thickness	d_{plate}	0.1×10^{-3}	m
Dust sample			
Initial density	ρ_i	300	kg m ⁻³
Bulk density	ρ_s	2000	kg m ⁻³
Reference density	ρ'_0	300	kg m ⁻³
Initial filling factor	ϕ_i	0.15	-
Bulk modulus	K_0	various	Pa
ODC mean pressure	p_m	260 and 1300	Pa
ODC max. filling factor	ϕ_2	0.58	-
ODC min. filling factor	ϕ_1	0.12	-
ODC slope	Δ	0.58	-
Impact velocity	v_0	0.2	m s ⁻¹
Radius	r	0.5×10^{-3}	m

Table 3. Numerical parameters for the bouncing calibration setup. ODC stands for omni-directional compression relation (Eq. 21). Quantities marked by (*) represent the parameters for sandstone in Melosh (1989), which we adopt for glass here.

(2009) with a rough model. Our simulations yield a coefficient of restitution $\epsilon_{\text{rest}} = 0.19$ ($\approx 96\%$ energy dissipation) for $K_0 = 5.0$ kPa, which is in excellent agreement with the experimental results. On the other hand for $K_0 = 500$ kPa we find $\epsilon_{\text{rest}} = 0.09$ ($\approx 99\%$ energy dissipation), which is too far away from the reference. A high value for the bulk modulus K_0 as it is given by the sound speed measurements is therefore excluded.

Given the higher value $p_m = 1.3$ kPa for the compressive strength curve ϵ_{rest} is raised for all choices of K_0 . For $K_0 = 1.0$ kPa it yields $\epsilon_{\text{rest}} \approx 0.7$ and only $\approx 50\%$ of the

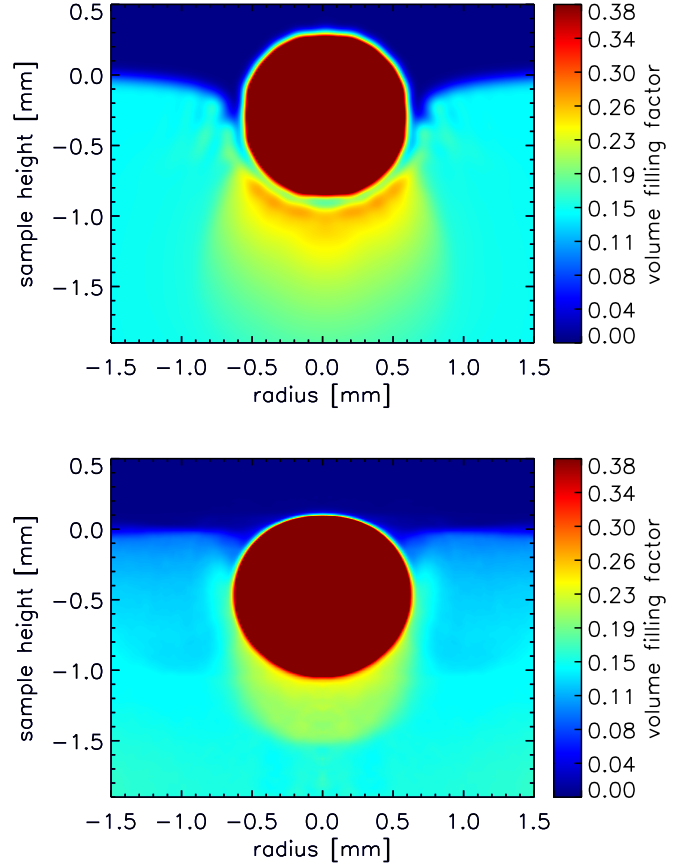


Fig. 16. Cross section through glass bead (red) and dust sample (light blue) at maximum intrusion for our 3D simulation (with $p_m = 0.26$ kPa, top) and the drop experiment (bottom). The colour indicates the spatially averaged filling factor. The density structure underneath the glass bead match very well. Even the slight compression along the tight intrusion channel can be reproduced. In the simulated plot a gap between glass bead and the most dense area is clearly visible. This is due to the smoothing of the sphere and was discussed in Sect. 4.2. The gap has roughly the size of one smoothing length h .

energy is dissipated. On the other hand for $K_0 = 300$ kPa we find $\epsilon_{\text{rest}} \approx 0.13$ equivalent to $\approx 98\%$ energy dissipation. For $p_m = 1.3$ kPa it is harder to dissipate energy by plastic deformation. Hence, less energy is dissipated in the compaction process and the coefficient of restitution is generally higher.

This bouncing experiment fixes our choice for the bulk modulus to $K_0 \approx 5$ kPa while maintaining $p_m = 0.26$ kPa from the compaction experiment in the previous section. The next section will show that this choice is also consistent with the fragmentation behaviour of the dust aggregates.

5.3. Fragmentation

Since the intended field of application of our calibrated SPH code will be the simulation of pre-planetesimal collisions, it is of major importance to calibrate and test the fragmentation behaviour of the simulated material. For this reason we simulate the fragmentation experiment described already in the second part of Sect. 3.3.

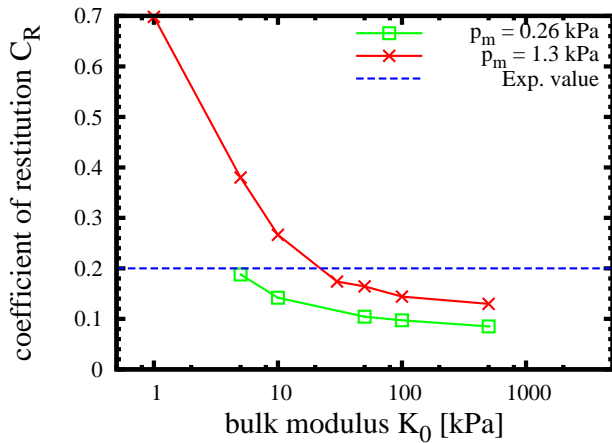


Fig. 18. Coefficient of restitution $\varepsilon_{\text{rest}}$ over bulk modulus K_0 for values of the mean pressure p_m of the compressive strength relation. For the lower $p_m = 0.26$ kPa (squares) more energy is dissipated by plastic deformation. For this reason the coefficient of restitution is significantly lowered compared to the higher $p_m = 1.3$ kPa (crosses). Best agreement with the experimental reference of $\varepsilon_{\text{rest}} = 0.2$ (dashed line) is given for $K_0 \approx 5$ kPa and $K_0 \approx 20$ kPa, respectively.

In our simulation a dust aggregate ($\phi_i = 0.35$, 189296 particles) hits a glass plate (188478 particles) from below with an impact velocity of $v_0 = 8.4 \text{ m s}^{-1}$. The spatial resolution ($l_c = 8.0 \mu\text{m}$, $h = 30.0 \mu\text{m}$) was chosen such that a single particle has less than 5×10^{-6} times the mass of the whole aggregate ($6.8 \times 10^{-8} \text{ kg}$) to resolve the same fragment masses as the experimental reference. Gravitation was taken into account. A list of the other relevant parameters can be found in Table 4.

We investigated the influence of the bulk modulus on the fragmentation behaviour. For this reason we varied K_0 from 3.0 kPa to 6.5 kPa. For comparison with the reference experiment (Fig. 2) we also plot our fragmentation data in a cumulative way (Fig. 19) and find also a good agreement with the power-law distribution of Eq. 24. The simulation was evaluated after 0.8 ms simulated time. The mass of a fragment is given by the sum of the mass of the SPH particles belonging to it. We consider two fragments as separated when they are not linked by SPH particles that interact with each other, i.e. when the closest SPH particles of two fragments have a distance more than a smoothing length.

Güttler et al. (2009b) were facing the problem that using $K_0 = 300$ kPa almost no fragmentation occurred (see Fig. 21 in this reference). Their speculations about a modification of the shear strength in order to resolve this problem proved to be wrong. The quantity with the most impact on the fragmentation behaviour of the dust aggregate is its bulk modulus. In general it can be said that an increase of the bulk modulus leads to an increasing slope α of the fragment distribution, whereas the size of the largest fragment (normalised through the total mass of the projectile) μ roughly remains constant at $\approx 20\%$ up to $K_0 = 6.0$ kPa. For higher K_0 mainly small chunks and single SPH particles will burst off the aggregate, which is only compacted but does not fragment. This reproduces the situation described in Güttler et al. (2009b) and Sect. 3.

We calibrate for α , which is more sensitive to changes of K_0 (see Table 5). Given the measured value of $\alpha = 0.67$ we find an excellent agreement with our simulation using $K_0 = 4.5$ kPa,

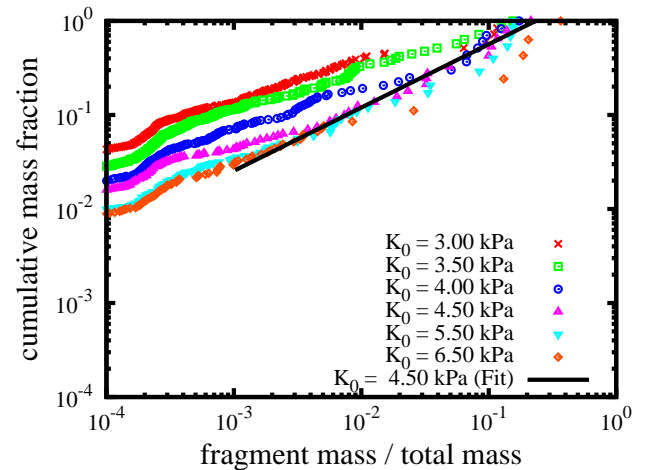


Fig. 19. Cumulative mass distribution of the fragments of a dust aggregate impacting on a glass plate for different values of K_0 . For low fragment masses the shape of all simulated curves differs from the experimental curve in Fig. 2 due to the limited resolution of the experimental setup. An increase of K_0 leads to an increase in the slope α of the power-law fit. The best agreement with the experimentally measured slope 0.67 was found for the simulation with $K_0 = 4.5$ kPa.

which yields $\alpha = 0.673 \pm 0.017$. Moreover this simulation reproduces also the experimentally measured normalised mass of the largest fragment $\mu = 0.22$ to a very high accuracy ($\mu = 0.234 \pm 0.007$). The slight overestimation may be caused by the fact that the increase in filling factor is not taken into account in the analysis of the experimental data (see Sect. 3), whereas in the simulation it is. The fragment distributions for different K_0 and the best fit for the power-law are shown in Fig. 19. Setup and outcome of the simulation are displayed in Fig. 20. As already indicated in Sect. 5.2 the choice of $p_m = 0.26$ kPa and $K_0 = 4.5$ kPa is consistent with the results from the compaction and bouncing experiments. The fragmentation experiment serves as a proof for the validity of these choices and also for the consistency of the underlying porosity model.

In contrast to the experiments we find no material sticking to the glass plate. This is not possible due to the setup of the simulation. As in Sect. 4.4 we use artificial viscosity to separate glass and dust materials. This leads to an additional pressure on the dust material which prevents sticking.

6. Discussion

In this work we presented a smooth particle hydrodynamics (SPH) code equipped with extensions for continuum mechanics of solid bodies and an extended version of the Sirono (2004) porosity model. The code uses experimentally measured macroscopic parameters such as tensile strength and a static compressive strength relation. In Güttler et al. (2009b) this code was used to determine a relation for the shear strength and an estimate for the mean pressure p_m for the dynamic compressive strength relation (Eq. 21). The estimate was quite crude, though, due to the usage of 2D simulations only.

This work profoundly investigated the numerical properties of the SPH code. Utilising the compaction calibration setup of Güttler et al. (2009b) as an example we determined an adequate size of the computational domain and adequate numerical and spatial resolutions. We have shown that the results for this setup

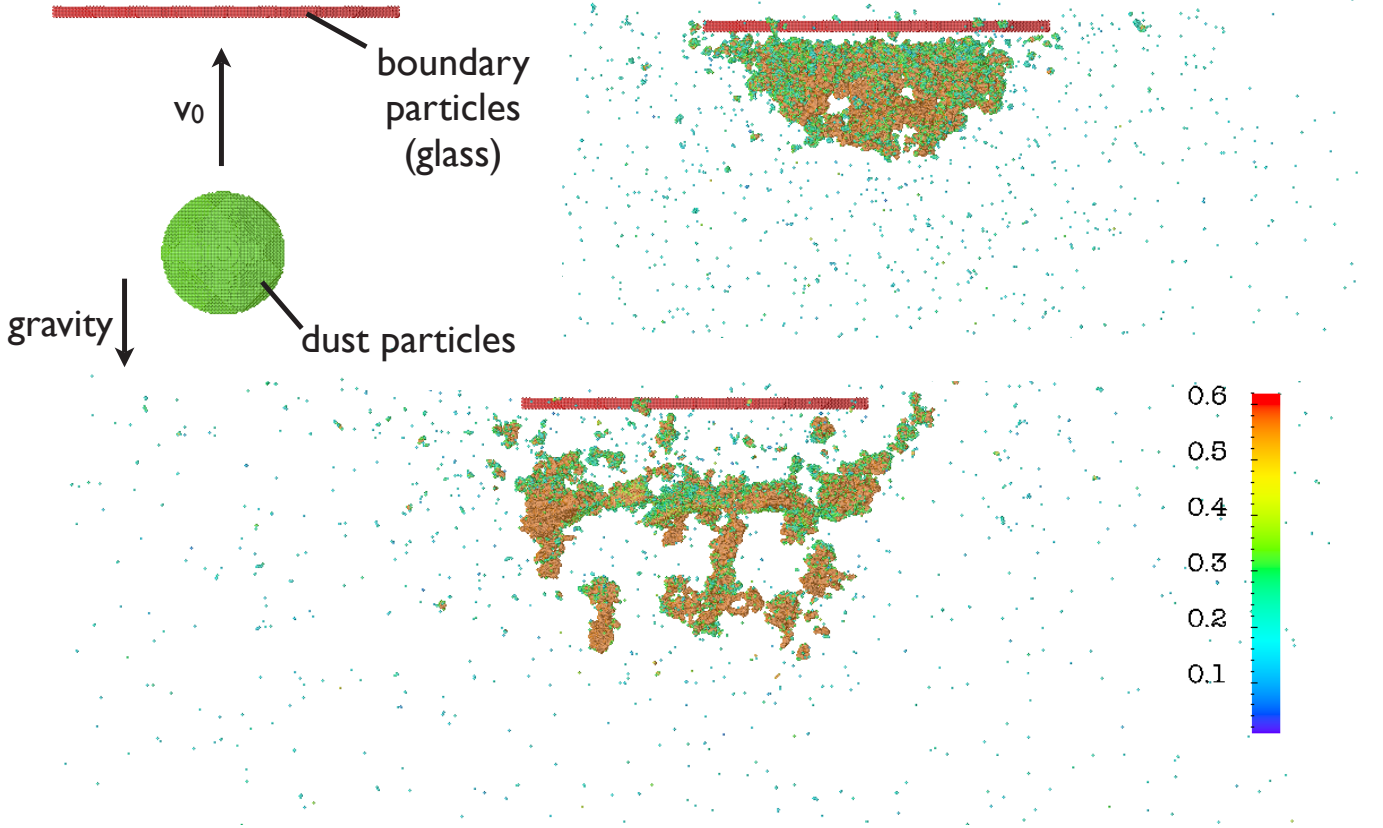


Fig. 20. Fragmentation sequence for $t = 0$ ms (top left), $t = 0.4$ ms (top right), and $t = 0.8$ ms (bottom). The colour code indicates the filling factor. A projectile consisting of dust particles (Sirono EOS, diameter 0.57 mm) hits a solid surface simulated by boundary glass particles (Murnaghan EOS, diameter 1.6 mm, thickness 0.04 mm) with an impact velocity of $v_0 = 8.4 \text{ m s}^{-1}$. A bulk modulus of $K_0 = 4.5 \text{ kPa}$ was used for this simulation. While many small pieces, often single SPH particles, chip off, most of the aggregate is compacted to its maximum filling factor $\phi_{\text{max}} = 0.58$ and fractures. The bottom layer of the impacting sphere is hardly compacted. This uncompacted layer is still visible on the fragments. (An animation of this figure is available in the online journal.)

Physical Quantity	Symbol	Value	Unit
Glass plate			
Bulk density ^(*)	ρ_0	2540	kg m^{-3}
Bulk modulus ^(*)	K_0	5×10^9	Pa
Murnaghan exponent ^(*)	n	4	-
Radius	r_{plate}	0.8×10^{-3}	m
Thickness	d_{plate}	0.04×10^{-3}	m
Dust sample			
Initial density	ρ_i	300	kg m^{-3}
Bulk density	ρ_s	2000	kg m^{-3}
Reference density	ρ'_0	700	kg m^{-3}
Initial filling factor	ϕ_i	0.35	-
Bulk modulus	K_0	various	Pa
ODC mean pressure	p_m	260	Pa
ODC max. filling factor	ϕ_2	0.58	-
ODC min. filling factor	ϕ_1	0.12	-
ODC slope	Δ	0.58	-
Impact velocity	v_0	8.4	m s^{-1}
Radius	r	0.285×10^{-3}	m

Table 4. Numerical parameters for the fragmentation calibration setup. ODC stands for omni-directional compression relation (Eq. 21). Quantities marked by (*) represent the parameters for sandstone in Melosh (1989), which we adopt for glass here.

K_0 [kPa]	Slope α	Norm. largest fragment μ
3.00	0.361 ± 0.004	0.200 ± 0.008
3.50	0.429 ± 0.002	0.172 ± 0.002
4.00	0.518 ± 0.011	0.230 ± 0.009
4.25	0.523 ± 0.006	0.194 ± 0.004
4.50	0.673 ± 0.017	0.234 ± 0.007
4.75	0.834 ± 0.025	0.196 ± 0.005
5.00	0.832 ± 0.063	0.198 ± 0.011
5.50	0.836 ± 0.052	0.220 ± 0.010
6.00	2.027 ± 0.121	0.171 ± 0.002
6.50	0.910 ± 0.053	0.390 ± 0.013

Table 5. Results from the fragmentation calibration setup. The slope α of the power-law is increasing with increasing bulk modulus K_0 . Remarkably, the size of the normalised biggest fragment remains nearly constant around $\mu \approx 0.2$ for $K_0 \leq 6.0 \text{ kPa}$.

are converging for higher spatial resolutions. Boundary conditions are necessary for all calibration setups presented in this work. Their treatment, which is a difficult issue in SPH, was resolved by using boundary particles with vanishing acceleration at every time step. The dissipative properties of the artificial viscosity and its role for the stability of the simulation were investigated. Artificial viscosity was used to separate dust and glass ma-

material which are highly different in the “stiffness” of their equations of state.

We investigated the crucial differences between 2D and 3D compaction calibration setup and proved the validity of the correction factor for the intrusion depth (Eq. 26) that was already used without confirmation in Güttler et al. (2009b). A major difference between experiments and simulations, a compaction that went too far down in the dust sample and along with this a compaction of too much volume, was resolved by using the 3D setup.

Using a series of 2D simulations of the compaction calibration setup we predicted a new, more accurate, value for the mean pressure p_m of the dynamic compressive strength relation. A 3D simulation with this value $p_m = 0.26$ kPa was carried out. The results were compared with the experimental reference using the same benchmark features as in Güttler et al. (2009b). We found a good agreement.

In Güttler et al. (2009b) it was already demonstrated that our code is in principle capable of simulating the bouncing of dust aggregates. With the bouncing calibration setup we now investigated the ability of the SPH code of quantitatively simulating the elastic properties of the dust and the energy dissipation by compaction. We found that the bulk modulus as well as the compressive strength relation have significant influence. For smaller values of p_m (low compressive strength) and higher values of the bulk modulus more energy is dissipated. Using $p_m = 0.26$ kPa from the compaction calibration setup we deduced that the uncompressed dust samples ($\phi \approx 0.15$) have a bulk modulus $K_0 \approx 5$ kPa. With this result we were able to decide between two differing experimental values in favour of the indirect determination by Weidling et al. (2009).

An important application of this code will be pre-planetesimal collisions. Therefore we also tested the code for its ability to simulate fragmentation of dust aggregates quantitatively correct. For this we used a fragmentation calibration setup and identified the bulk modulus as the quantity with the most influence on the fragment distribution. Again using $p_m = 0.26$ kPa from the compaction calibration setup we found the best agreement with the empirical reference for the bulk modulus $K_0 = 4.5$ kPa. Remarkably this is consistent with the findings from the bouncing calibration setup, which represents a test for a totally different behaviour. The problem of almost no fragmentation for $K_0 = 300$ kPa described in Güttler et al. (2009b) was hereby traced back to a wrong assumption for the bulk modulus.

7. Conclusion

Schäfer et al. (2007) have shown that the outcome of pre-planetesimal collisions crucially depend on their material properties. If the issue of collisional growth is to be investigated by computer simulations, they suggest an implementation of experimentally measured material parameters and thorough calibration and comparison with laboratory experiments.

The SPH code presented in this work complies with their requirements. Based on the experimental preparatory work by Güttler et al. (2009b) this code has been successfully tested with three kinds of calibration setups for the correct simulation of compaction, bouncing, and fragmentation.

We conclude that we have developed a tool that features a sufficient accuracy for the investigation of the outcome of pre-planetesimal collisions in parameter ranges that are not accessible to laboratory experiments. This is based on the assumption that the macroscopic properties calibrated for in this work do not change with increasing size. However, due to the thermodynamically simple porosity model used in the SPH code the area of

application is restricted to a certain range of collision velocities. Collisions where shock propagation cannot be neglected are outside the physically meaningful limit of this model. Changes of the mechanical properties with temperature and other thermodynamical effects like sintering and melting cannot be simulated. An extension of the porosity model and its implementation and calibration are necessary to broaden the parameter range (e.g. supersonic impacts) and to consider a realistic environment for pre-planetesimal collisions in the protoplanetary disc.

Nevertheless, within its area of application our code will be used to produce a “catalogue of collisions”. The influence of object sizes, porosity, relative velocity, rotation, and impact parameter on the fragment distribution of pre-planetesimal collisions will be investigated in future work.

Acknowledgements. The authors want to thank Serena E. Arena for many fruitful discussions and helpful comments about the manuscript. The SPH simulations were performed on the university and bwGrid clusters of the computing centre (ZDV) of the University of Tübingen. We thank M.-B. Kallenrode and the University of Osnabrück for providing access to the XRT setup. We also thank the anonymous referee for clarifying comments and suggestions. This project was funded by the Deutsche Forschungsgemeinschaft within the Forschergruppe 759 “The Formation of Planets: The Critical First Growth Phase” under grants BI 298/7-1, BI 298/8-1, and KI 650/8-1.

References

- Benz, W. & Asphaug, E. 1994, *Icarus*, 107, 98
 Benz, W. & Asphaug, E. 1995, *Computer Physics Communications*, 87, 253
 Blum, J. & Münch, M. 1993, *Icarus*, 106, 151
 Blum, J. & Schräpler, R. 2004, *Phys. Rev. Lett.*, 93, 115503
 Blum, J., Schräpler, R., Davidsson, B. J. R., & Trigo-Rodríguez, J. M. 2006, *ApJ*, 652, 1768
 Blum, J. & Wurm, G. 2000, *Icarus*, 143, 138
 Blum, J. & Wurm, G. 2008, *ARA&A*, 46, 21
 Blum, J., Wurm, G., Kempf, S., et al. 2000, *Physical Review Letters*, 85, 2426
 Brauer, F., Dullemond, C. P., & Henning, T. 2008, *A&A*, 480, 859
 Davis, D. R. & Ryan, E. V. 1990, *Icarus*, 83, 156
 Dominik, C. & Tielens, A. G. G. M. 1997, *ApJ*, 480, 647
 Dullemond, C. P. & Dominik, C. 2005, *A&A*, 434, 971
 Geretshauer, R. 2006, Master’s thesis, Eberhard-Karls-Universität Tübingen
 Gingold, R. A. & Monaghan, J. J. 1977, *MNRAS*, 181, 375
 Grady, D. E. & Kipp, M. E. 1980, *Int. J. Rock Mech. Min. Sci. Geomech. Abstr.*, 17, 147
 Güttler, C., Blum, J., Zsom, A., Ormel, C. W., & Dullemond, C. P. 2009a, *A&A*, submitted
 Güttler, C., Krause, M., Geretshauer, R. J., Speith, R., & Blum, J. 2009b, *ApJ*, 701, 130
 Heim, L.-O., Blum, J., Preuss, M., & Butt, H.-J. 1999, *Physical Review Letters*, 83, 3328
 Heißelmann, D., Fraser, H., & Blum, J. 2007, in *Proceedings of the 58th International Astronautical Congress 2007, IAC-07-A2.1.02*
 Jutzi, M. 2008, PhD thesis, Universität Bern
 Jutzi, M., Benz, W., & Michel, P. 2008, *Icarus*, 198, 242
 Jutzi, M., Michel, P., Benz, W., & Richardson, D. C. 2009a, *MNRAS*, submitted
 Jutzi, M., Michel, P., Hiraoka, K., Nakamura, A. M., & Benz, W. 2009b, *Icarus*, in press
 Krause, M. & Blum, J. 2004, *Physical Review Letters*, 93, 021103
 Libersky, L. D. & Petschek, A. G. 1990, in *Advances in the Free-Lagrange Method*, ed. H. E. Trease, M. J. Fritts, & W. P. Crowley (Springer Verlag), 248–257
 Libersky, L. D., Petschek, A. G., Carney, T. C., Hipp, J. R., & Allahdadi, F. A. 1993, *J. Chem. Phys.*, 109, 67
 Libersky, L. D., Randles, P. W., Carney, T. C., & Dickinson, D. L. 1997, *Int. J. Impact Eng.*, 20, 525
 Lucy, L. B. 1977, *ApJ*, 82, 1013
 Mathis, J. S., Rumpl, W., & Nordsieck, K. H. 1977, *ApJ*, 217, 425
 Melosh, H. J. 1989, *Oxford monographs on geology and geophysics*, Vol. 11, *Impact cratering: A geologic process*, ed. H. J. Melosh (Oxford University Press)
 Monaghan, J. J. 2005, *Reports on Progress in Physics*, 68, 1703
 Monaghan, J. J. & Gingold, R. A. 1983, *J. Chem. Phys.*, 52, 374
 Monaghan, J. J. & Lattanzio, J. C. 1985, *A&A*, 149, 135
 Omang, M., Børve, S., & Trulsen, J. 2006, *Journal of Computational Physics*, 213, 391

- Ormel, C. W., Paszun, D., Dominik, C., & Tielens, A. G. G. M. 2009, *A&A*, 502, 845
- Ormel, C. W., Spaans, M., & Tielens, A. G. G. M. 2007, *A&A*, 461, 215
- Paszun, D. & Dominik, C. 2006, *Icarus*, 182, 274
- Paszun, D. & Dominik, C. 2008, *A&A*, 484, 859
- Paszun, D. & Dominik, C. 2009, *A&A*, 507, 1023
- Randles, P. W. & Libersky, L. D. 1996, *Comp. Methods Appl. Mech. Engrg.*, 139, 375
- Schäfer, C., Speith, R., & Kley, W. 2007, *A&A*, 470, 733
- Sirono, S.-I. 2004, *Icarus*, 167, 431
- Teiser, J. & Wurm, G. 2009, *MNRAS*, 393, 1584
- Wada, K., Tanaka, H., Suyama, T., Kimura, H., & Yamamoto, T. 2007, *ApJ*, 661, 320
- Wada, K., Tanaka, H., Suyama, T., Kimura, H., & Yamamoto, T. 2008, *ApJ*, 677, 1296
- Wada, K., Tanaka, H., Suyama, T., Kimura, H., & Yamamoto, T. 2009, *ApJ*, in press
- Weidenschilling, S. J. 1977, *MNRAS*, 180, 57
- Weidenschilling, S. J. & Cuzzi, J. N. 1993, in *Protostars and Planets III*, ed. E. H. Levy & J. I. Lunine, 1031–1060
- Weidenschilling, S. J., Spaute, D., Davis, D. R., Marzari, F., & Ohtsuki, K. 1997, *Icarus*, 128, 429
- Weidling, R., Güttler, C., Blum, J., & Brauer, F. 2009, *ApJ*, 696, 2036
- Wurm, G., Paraskov, G., & Krauss, O. 2005, *Icarus*, 178, 253
- Zsom, A. & Dullemond, C. P. 2008, *A&A*, 489, 931
- Zsom, A., Ormel, C. W., Güttler, C., Blum, J., & Dullemond, C. P. 2009, *A&A*, submitted